Investigation of Organic ETLs in QLEDs and a Metal-based RGB Patterning Technique for QLED Displays

by

Bhuiyan Saad Bin Mobarak

A thesis

presented to the University of Waterloo

in fulfillment of the

thesis requirement for the degree of

Master of Applied Science

in

Electrical and Computer Engineering (Nanotechnology)

Waterloo, Ontario, Canada, 2025

© Bhuiyan Saad Bin Mobarak 2025

Author's Declaration

I hereby declare that I am the sole author of this thesis. This is a true copy of the thesis, including any required final revisions, as accepted by my examiners.

I understand that my thesis may be made electronically available to the public.

Abstract

Colloidal quantum dot light-emitting devices (QLEDs) have attracted significant interest for next-generation emissive display and lighting applications owing to their narrowband emission, tunable bandgaps, and compatibility with solution-based fabrication. Their emissive layers (EMLs), composed of colloidal quantum dots (QDs), exhibit discrete energy states and size-dependent bandgaps, allowing precise spectral tunability and narrow emission linewidths (FWHM < 25 nm). The high photoluminescence quantum yield (PLQY), excellent photochemical stability, and compatibility with low-temperature fabrication processes make them highly suitable for large-area and flexible devices. Collectively, these properties position QLEDs as strong contenders to replace organic-LEDs (OLEDs) in future display technologies, offering improved color saturation, reduced power consumption, and enhanced manufacturing versatility.

Despite these advantages, QLEDs still face fundamental challenges related to charge transport and device efficiency. In particular, the use of organic electron transport layers (ETLs) has been limited due to their perceived low electron mobility and inferior performance compared to inorganic metal-oxide ETLs. However, organic ETLs remain attractive for certain device architectures because of their solution processability, tunable energy levels, and compatibility with low-temperature and flexible fabrication. Moreover, organic layers can form smoother, defect-free interfaces with the QD EMLs compared to metal-oxide ETLs, which may introduce interfacial traps or cause damage during deposition. While the low efficiency of QLEDs employing organic ETLs has conventionally been attributed to their poor electron mobility, the findings presented in this thesis reveal that uncontrolled electron leakage from the QD EML to the hole transport layer (HTL) plays a more dominant role. Based on the finding, the design and optimization of multilayer organic ETL architectures with electron-blocking interfaces effectively suppress electron leakage, leading to improved charge balance and enhanced device efficiency. Using this approach, both red

and green QLEDs achieve maximum EQEs approaching 10%, representing among the highest reported values for devices employing organic ETLs.

Another limitation in QLEDs is their limited amenability to high-resolution patterning of RGB arrays for full-color displays. Conventional techniques, such as inkjet printing or photolithography, often suffer from limited resolution, QD degradation, or complex processing steps that can compromise device performance. This thesis also presents a novel RGB patterning technique based on metal-induced quenching. Thin metal layers are selectively deposited via a shadow mask onto target areas of the QD EMLs, where subsequent metal diffusion into the EML locally suppresses luminescence through non-radiative energy transfer, while unexposed regions retain their intrinsic emission characteristics. Optical and morphological characterization shows that metal-coated QD regions develop increased surface roughness and island-like features, indicating that metal diffusion into the QD layer plays a significant role in facilitating non-radiative quenching. Using this approach, we demonstrate the fabrication of devices containing multiple QLEDs from a single multilayer stack, each producing spectrally pure electroluminescence (EL) without detectable parasitic emission. Additional patterned structure demonstrates controlled microscale emission at the device level, establishing the feasibility of achieving spatial color definition with high precision. These results validate metal-induced quenching as an effective methodology for QLED color patterning and provide insight into metal-QD interactions.

Acknowledgements

First and foremost, I would like to thank Almighty Allah for His countless blessings, guidance, and mercy throughout my life and especially during my MASc journey. His guidance and blessings have been my constant source of strength, helping me persevere through challenges and reach this important milestone in my life.

I am deeply grateful to my supervisor, Professor Hany Aziz, for his unwavering guidance, support, patience, and encouragement throughout my MASc. He welcomed me into his group even though I had no prior experience or knowledge in semiconductors or optoelectronic device fabrication and characterization. Whenever I approached him for a discussion, he was always pleased to take his time out. He provided clear research directions, valuable feedback, and consistent support that allowed me to develop my skills, gain confidence, and grow as a researcher. I have learned so much from him - from designing experiments to writing and presenting scientific work, lessons that have shaped both my research abilities and personal growth. I will always be indebted to him for his trust, guidance, and inspiration. Words cannot fully express my gratitude for his unwavering support and guidance throughout my journey at the University of Waterloo.

I would like to sincerely thank Dr. Guo-Xing Miao and also Dr. Yuning Li for agreeing to serve as a reader of my thesis. Your feedback and support have been invaluable and greatly appreciated.

I am also thankful to all my group members, who made the lab an inspiring and enjoyable place to work. From them, I have learned not only technical skills but also the true value of teamwork, resilience, and creative problem-solving. Their guidance, encouragement, and camaraderie have enriched my research experience and made my MASc journey more meaningful.

I owe a special debt of gratitude to my family. To my parents, whose love, guidance, and sacrifices have shaped me into the person I am today. To my sisters, Mishe and Muna, and my brothers-in-law, for their support, encouragement, and care. To my father Mobarak, whose example, values, and unwavering belief in me have been a constant source of strength and inspiration.

I want to express my deepest gratitude to my wife, Nabila, my best friend, soulmate, and constant support. Her love, encouragement, and understanding have been my anchor through the highs and lows of this journey. She has always believed in me, lifted me when I doubted myself, and celebrated every

achievement along the way. Nabila, I cannot thank you enough for being by my side. Your presence and love have made this journey possible and meaningful.

Finally, I am eternally grateful to my mother, Asma. Without her prayers, guidance, and unwavering support, I would not have reached this milestone. Her love has been my anchor through every challenge, and her belief in me has never wavered, even in moments when I doubted myself. From my earliest steps to this moment, she has always been my source of strength, offering encouragement, wisdom, and comfort in every phase of my life. Her sacrifices, patience, and constant care have shaped me into the person I am today, and her words have inspired me to persevere when the path seemed difficult. I owe all my achievements to her endless love, devotion, and faith in me. She has truly been my guiding light and my greatest inspiration.

Table of Contents

Author's Declaration ii

Abstract iii

Acknowledgements v

List of Figures ix

List of Tables xi

List of Abbreviations xii

Chapter 1. Introduction 1

1.1 Colloidal Quantum Dots 1

1.2 Quantum Dot LEDs (QLEDs) 4

1.2.1 QLEDs Structures: 4

1.2.2 Common Materials in QLEDs: 5

1.2.3 Applications & Advantages: 7

1.3 RGB Patterning 9

1.4 Challenges in QLEDs 11

1.4.1 ZnO/ZnMgO - Ubiquitousness and Limitations 11

1.4.2 RGB Patterning via Inkjet – Limitations 11

1.5 Thesis Organization 12

Chapter 2. Literature Review 13

2.1 Electron Transport Layers in QLEDs 14

2.1.1 ZnO/ZnMgO ETLs 14

2.1.2 Alternative ETLs 16

2.2 Patterning Techniques in QLEDs 17

2.2.1 Inkjet Printing 17

2.2.2 Other Patterning Techniques 19

2.2.3 Concept of RGB Patterning by Metal Quenching 21

2.3 Conclusion 24

Chapter 3. Research Objectives & Methodology 25

3.1 Research Objectives 25

3.1.1 Understanding and Overcoming the Poor Efficiency of QLEDs Utilizing Organic ETLs. 25

3.1.2 Testing the feasibility of RGB Color Patterning in QLED Panels via Quenching by Metals via a Shadow Mask. 26

3.2 Research Methodology 26

3.2.1 Device Layout 26
3.2.2 Device Fabrication 27
3.2.3 Device Characterization 30
3.2.4 Materials 30
Chapter 4. Understanding and Overcoming the Poor Efficiency of QLEDs Utilizing Organic Electron Transport Layers 32
4.1 Results & Discussion 32
4.2 Conclusion 51
Chapter 5. Testing the Feasibility of RGB Color Patterning in QLED Panels via Quenching by Metals via the Use of a Shadow Mask 53
5.1 Results & Discussion 54
5.2 Conclusion 67
Chapter 6. Conclusions & Recommendations for Future Work 69
6.1 Summary of Main Conclusions 69
6.2 Recommendations for Future Work 70
References 73

List of Figures

Figure 1.1 Structure of QDs comprising a core, shell, and ligands [6]..... 2
Figure 1.2. Schematic showing how QD size affects emission. Electrons excited from the valence to conduction band emit light; smaller QDs (wider band gaps) emit shorter wavelengths, while larger QDs (narrower band gaps) emit longer wavelengths. [13]..... 3
Figure 1.3. Schematic illustration of (a) upright and (b) inverted QLED architectures. 5
Figure 1.4. Energy levels of materials commonly used in the fabrication of QLEDs [27]..... 6
Figure 1.5. RGB approaches for OLED displays: a) side-by-side RGB OLEDs, b) white OLEDs plus CFs, and c) blue OLEDs with CCMs. [39] 10
Figure 2.1. General schematic of the inkjet printing process in QLEDs. [73] 18
Figure 2.2. Schematic illustration of RGB color patterning in QLEDs, where sequentially deposited QD emissive layers are selectively quenched by vacuum-deposited metals in defined areas, resulting in blue, green, and red emission from different areas of the stacked device under applied bias. 22
Figure 3.1. Schematic of the QLED substrate layout used in this study..... 27
Figure 4.1. (a) A schematic diagram of the green QLED structure, (b) Molecular structures of the B3PYMPM & B4PYPPM, (c) J-V characteristics, (d) EQE vs J characteristics, and (e) Normalized EL spectra of QLEDs with the two different organic ETLs. 34
Figure 4.2. (a) J-V characteristics, (b) EQE vs J characteristics, (c) Normalized EL spectra, and (d) Leakage coefficient of devices with double ETLs of various layers thicknesses. Characteristics from the single layer are also included for comparison. 37
Figure 4.3. (a) J-V characteristics (b) EQE vs J, and (c) Normalized EL spectra of 10nm/30nm double ETL devices without and with the CBP layer. 40
Figure 4.4. (a) Schematic diagrams showing the structures of the EODs with and without CBP, and (b) J-V characteristics of the same EODs. 42
Figure 4.5. TREL spectra measured under pulsed current with varying pulse durations for the QLEDs with; (a) B3PYMPM single layer ETL, (b) B4PYMPM single layer ETL, (c) double layer (10nm/30nm) ETL, and (d) triple layer (CBP/10nm/30nm) ETL. 44
Figure 4.6. A graphical representation of a possible model for the reduced electron leakage and higher EQE of the devices with the double and triple ETLs depicting differences in charge injection

and transport between the QLEDs containing (a) single layer, (b) double layer, and (c) triple layer ETLs. The numbers in the squares refer to the following processes or phenomena whereas the line width of the different arrows represent their relative magnitude where applicable [i] Electron supply to the QD EML, [ii] Electron leakage from QD EML to HTL, [iii] Hole injection at the HTL/QD EML interface, [iv] Hole accumulation at the HTL/QD EML interface, [v] Electron injection between ETLs, and [vi] Electron accumulation at ETL interfaces. 46
Figure 4.7. J-V measurements of the fabricated triple layer (CBP/10nm/30nm) organic ETLs structure done after 0 hour, 24 hours and 72 hours. 48
Figure 4.8. (a) J-V-L characteristics, (b) EQE vs J characteristics, and (c) Normalized EL spectra of the red, green and blue QLEDs with the organic ETLs..... 50
Figure 5.1. (a) Graphical representation of metal-induced QD quenching, (b) PL spectra, and (c) TrPL decay characteristics of Glass/R-QDs and Glass/R-QDs/Ag films under 365 nm excitation 55
Figure 5.2. Transmittance analysis of the Glass/Ag and the Glass/R-QDs/Ag films. 56
Figure 5.3. (a, b) AFM top-view, (c, d) AFM 3D, and (e, f) SEM images comparing the surface morphology of Glass/Ag and Glass/R-QDs/Ag films respectively. 58
Figure 5.4. Process of the RG QLED fabrication. 60
Figure 5.5. (a) J-V-L, (b) Normalized EL and (c) Normalized PL spectra collected from the two different QLEDs from the same QD layer stack. 62
Figure 5.6. Structure of the RGB hybrid device (R, G QLEDs and B-OLED) 63
Figure 5.7. (a) EL image, (b) PL image under UV lamp of the full RGB hybrid device, (c) CIE color index of the devices (for Red X: 0.673 and Y: 0.326, for Green X: 0.195 and Y: 0.776, and for Blue X: 0.165 and Y: 187), (d) Normalized EL, and (e) Normalized PL spectra of these devices. 65
Figure 5.8. Patterned devices showing (a) side-by-side integration of red and green QLED emissive areas within a single device, and (b) side-by-side integration of red QLEDs with blue OLEDs. 66

List of Tables

Table 4.1. Driving voltages, luminance at 20 mA/cm², and max EQE values for the investigated devices..... 38
Table 4.2. Luminance values of the triple layer (CBP/10nm/30nm) organic ETLs structure measured after 0 hour, 24 hours and 72 hours 49
Table 4.3. Measured performance parameters of Red, Green, and Blue QLEDs with organic ETLs..... 51
Table 5.1. RMS values and height difference between the lowest and the highest point in the surface. 59

List of Abbreviations

AFM: Atomic Force Microscopy

Alq_3: Tris(8-hydroxyquinoline)aluminum

B3PYMPM: Spiro-2CBP, 4,6-Bis(3,5-di(pyridin-3-yl)phenyl)-2-methylpyrimidine

B4PYPPM: 4,6-Bis(3,5-di(pyridin-4-yl)phenyl)-2-phenylpyrimidine

BCzVBi: 4,4'-Bis(9-ethyl-3-carbazovinylene)-1,1'-biphenyl

BPhen: Bathophenanthroline

CB: Conduction Band

CBM: Conduction Band Minimum

CBP: 4,4′-Bis(N-carbazolyl)-1,1′-biphenyl

CCM: Color Conversion Media

CdS: Cadmium Sulfide

CdSe: Cadmium Selenide

CF: Color Filter

CTL: Charge Transport Layers

$CsPbX_3$: Cesium Lead Halide

E_g: Bandgap

EHD: Electrohydrodynamic

EL: Electroluminescence

EML: Emissive Layer

EOD: Electron Only Device

EQE: External Quantum Efficiency

ETL: Electron Transport Layer

FMM: Fine Metal Mask

FPD: Flat Panel Display

FRET: Förster Resonance Energy Transfer

FWHM: Full Width at Half Maximum

HOMO: Highest Occupied Molecular Orbital

HIL: Hole Injection Layer

HTL: Hole Transport Layer

InAs: Indium Arsenide

InP: Indium Phosphide

ITO: Indium Tin Oxide

I-V: Current-Voltage

J-V: Current Density-Voltage

J-V-L: Current Density-Voltage-Luminance

LCD: Liquid Crystal Displays

LiF: Lithium Fluoride

LIFT: Laser-induced Forward Transfer

LUMO: Lowest Unoccupied Molecular Orbital

MO: Metal Oxide

MoO_3: Molybdenum Trioxide

NP: Nanoparticle

OLED: Organic Light Emitting Device

PEDOT:PSS: Poly(3,4-ethylenedioxythiophene)-poly(styrenesulfonate)

PEI: Polyethylenimine

PEIE: Polyethylenimine Ethoxylated

PMAH: Phosphomolybdic Acid Hydrate

Poly-TPD: Poly[N,N'-bis(4-butylphenyl)-N,N'-bis(phenyl)-benzidine]

PL: Photoluminescence

PLQY: Photoluminescence Quantum Yield

PVK: Poly(9-vinylcarbazole)

QD: Quantum Dot

QLED: Quantum Dot Light Emitting Device

RGB: Red, Green & Blue

SEM: Scanning Electron Microscopy

TBADN: 2-tert-Butyl-9,10-di(naphth-2-yl)anthracene

TcTa: 4,4',4-Tris(carbazol-9-yl)triphenylamine

TFB: Poly[(9,9-dioctylfluorenyl-2,7-diyl)-co-(4,4'-(N-(4-sec-butylphenyl)diphenylamine)]

TFT: Thin Film Transistor

TmPyPB: 1,3,5-Tri[(3-pyridyl)-phen-3-yl]benzene

TOPO: Trioctylphosphine Oxide

TPBi: 1,3,5-Tris(1-phenyl-1Hbenzimidazol-2-yl)benzene

TrEL: Transient Electroluminescence

TrPL: Transient Photoluminescence

VB: Valence Band

V_{on}: Turn-on Voltage

V_{th}: Threshold Voltage

UHD: Ultra-High-Definition

ZnMgO: Zinc Magnesium Oxide

ZnS: Zinc Sulfide

ZnSe: Zinc Selenide

Chapter 1
Introduction & Background

1.1 Colloidal Quantum Dots

Colloidal Quantum dots (QDs) are semiconductor nanocrystals typically ranging from 2 to 10 nm in diameter, exhibiting discrete electronic states due to spatial confinement of charge carriers. A typical QD consists of a semiconductor core, an inorganic shell, and organic surface ligands. Figure 1.1 shows the schematic structure of QDs. The core material determines the bandgap and emission wavelength, while the shell serves to passivate surface traps, reduce non-radiative recombination, and improve Photoluminescence Quantum Yield (PLQY) [1, 2]. Commonly used core materials include II-VI compounds such as Cadmium Selenide (CdSe), Cadmium Sulfide (CdS), and Zinc Selenide (ZnSe), as well as III-V semiconductors such as Indium Phosphide (InP), which offer cadmium-free alternatives with lower toxicity [1] [3, 4]. The shell is typically composed of a wide-bandgap semiconductor such as Zinc Sulfide (ZnS) or ZnSe to provide carrier confinement and chemical stability [2]. The outer ligand layer, consisting of long-chain organic molecules such as oleic acid, trioctylphosphine oxide (TOPO), or amine-based species, stabilizes the QDs in colloidal form and prevents aggregation. However, these long-chain ligands hinder charge transport when QDs are deposited as solid films. To address this limitation, ligand exchange methods are employed to replace the native ligands with shorter organic or inorganic species, improving electronic coupling between adjacent QDs [5].

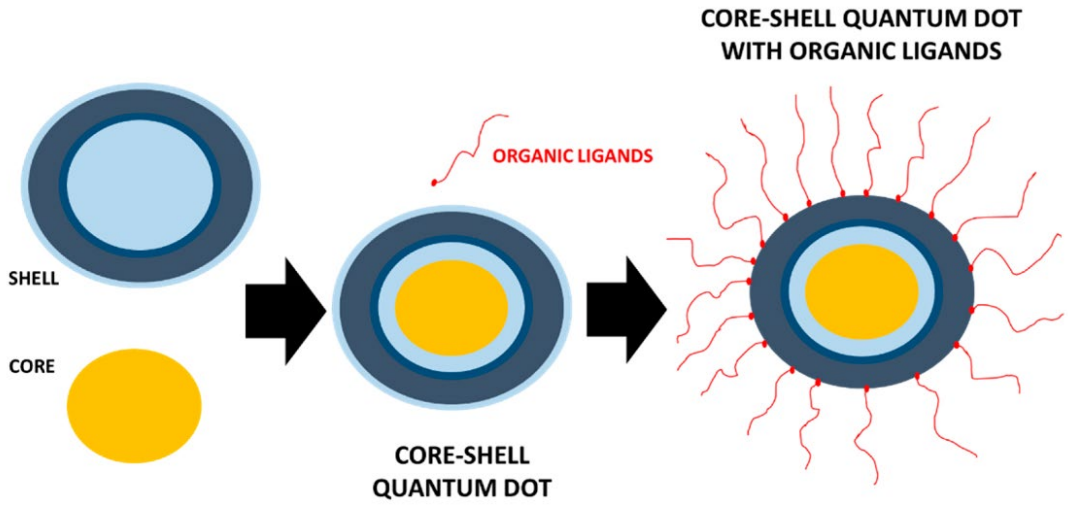


Figure 1.1 Structure of QDs comprising a core, shell, and ligands [6]

Advances in compositional and structural design have enabled high-performance QDs with improved photostability and emission uniformity. Alloyed and gradient core-shell structures, such as $CdSe_xS_{1-x}$ or InP/ZnSeS, reduce lattice mismatch and suppress Auger recombination, resulting in higher PLQY and narrower emission linewidths [7]. More recently, halide perovskite nanocrystals (e.g., Cesium Lead Halide ($CsPbX_3$), X = Cl, Br, I) have emerged as an alternative class of QDs offering high color purity and facile spectral tunability [8].

When the dimensions of a QD approach or fall below the exciton Bohr radius of its bulk semiconductor, the energy levels become quantized, leading to a size-dependent bandgap (E_g). As the QD size increases, the bandgap between the conduction band (CB) and valence band (VB) becomes smaller. This means that smaller QDs have larger bandgaps and emit light at shorter wavelengths (blue region), while larger QDs have smaller bandgaps and emit at longer wavelengths (red region), as shown in Figure 1.2 [9, 10]. This phenomenon originates from the quantum confinement effect, in which the motion of charge carriers is spatially restricted within

smaller QDs, resulting in discrete, quantized energy levels and tunable optical transitions [11, 12]. The extent of confinement directly influences the electronic structure and emission characteristics of QDs, making this effect a fundamental principle governing their optical and electronic behavior.

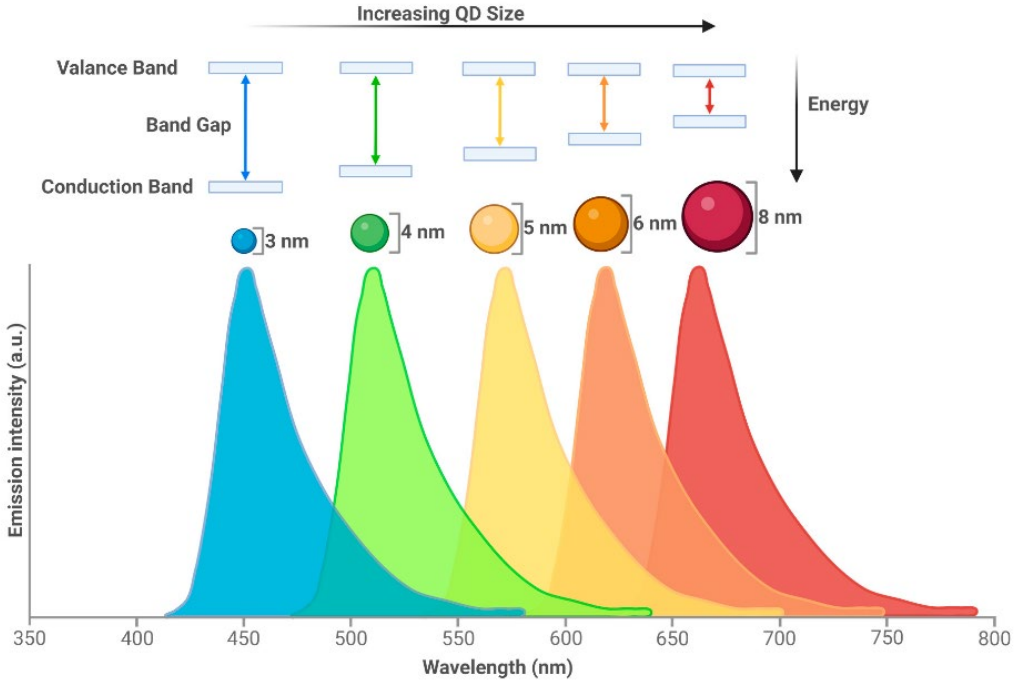


Figure 1.2. Schematic showing how QD size affects emission. Electrons excited from the valence to conduction band emit light; smaller QDs (wider band gaps) emit shorter wavelengths, while larger QDs (narrower band gaps) emit longer wavelengths. [13]

The capability to tune emission wavelength through particle size and composition, combined with their solution processability, allows QDs to be integrated into thin-film device structures using low-temperature fabrication methods. These characteristics provide the foundation for their implementation in QD based Light-Emitting Devices (QLEDs), where QDs act as the primary electroluminescent layer.

1.2 Quantum Dot LEDs (QLEDs)

QLEDs are electroluminescent devices that utilize colloidal QDs as the emissive layer (EML). In these devices, luminescence is produced by QDs due to the recombination of electrons and holes that are supplied to them from two electrodes, an anode and cathode, under an external electrical bias. The performance of QLEDs is directly linked to the intrinsic optical properties of QDs, which are determined by quantum confinement effects. In QLEDs, the discrete energy levels of QDs lead to narrow and size-tunable electroluminescence (EL) spectra, allowing precise control over emission wavelength and color purity [14, 15]. The narrow emission bandwidths, typically below 30 nm full width at half maximum (FWHM), contribute to high color saturation and a broad achievable color gamut, which are important metrics for display applications [16, 17].

1.2.1 QLEDs Structures:

The typical upright device architecture comprises several functional layers: a transparent substrate, an anode (commonly indium tin oxide, (ITO)), a hole injection layer (HIL), a hole transport layer (HTL), the QD EML, an electron transport layer (ETL), and a cathode. Each layer serves a specific function to facilitate efficient charge injection and transport, as well as to ensure effective light emission [18]. For instance, the HIL and HTL are responsible for hole injection and transport, while the ETL ensures electron injection and transport. The QD EML is where the recombination of electrons and holes occurs, leading to light emission [19].

Inverted QLEDs, where the layer sequence is reversed, have been developed to address issues such as charge imbalance and to enhance device stability. In this configuration, the cathode is positioned beneath the ETL, and the anode is placed on top of the HIL/HTL. This inversion can lead to improved charge injection balance, reduced interfacial degradation, and enhanced operational lifetime [20, 21]. Moreover, the inverted structure is more compatible with flexible substrates, which is advantageous for applications in

flexible and wearable electronics [21]. Figure 1.3 depicts the structural difference between upright and inverted QLED architectures, where the order of the transport layers and electrodes is reversed.

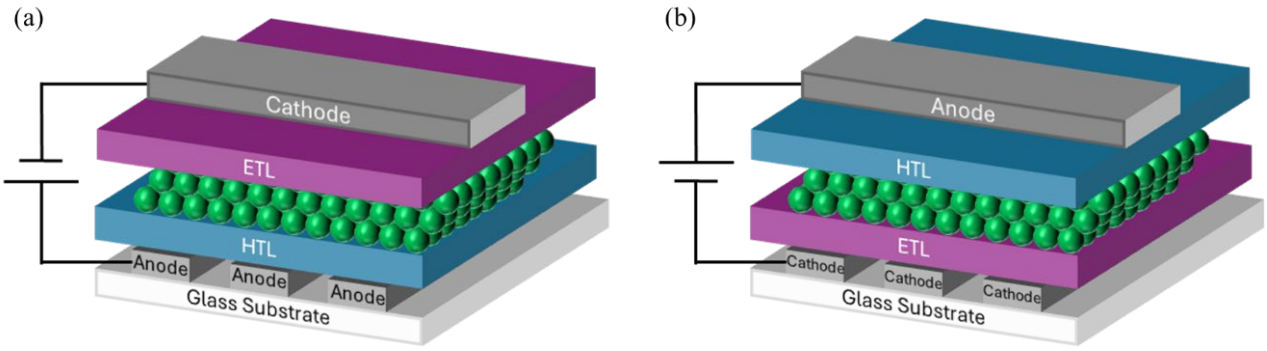


Figure 1.3. Schematic illustration of (a) upright and (b) inverted QLED architectures.

1.2.2 Common Materials in QLEDs:

To obtain highly efficient and stable QLEDs, careful selection of appropriate materials for the QDs-EML, ETL, HIL, and HTL is required. Figure 1.4 shows the energy levels of materials commonly used in the fabrication of QLEDs. QDs functioning as the EML are important to the device, hence their composition, shell architecture, and surface chemistry significantly affect electroluminescence efficacy and durability. Among colloidal QDs, CdSe/ZnS core/shell structures remain among the most widely employed in high-performance QLEDs because the lattice matching at the core/shell interface is favorable and allows for high PLQY and stability [22, 23]. For instance, a thick-shell, graded CdSe@ZnS/ZnS QD showed a PLQY of ~88 % and maintained only ~7 % drop in PL intensity after 400 hours of accelerated aging at 85 °C/85 % relative humidity [24]. Despite a significant emphasis on III-V (InP, Indium Arsenide (InAs)) or other Cd-free QDs due to toxicity issues, these alternatives frequently exhibit poorer PLQY yields or present greater challenges in synthetic control, hence constraining their widespread implementation in high-efficiency QLEDs to date [25, 26].

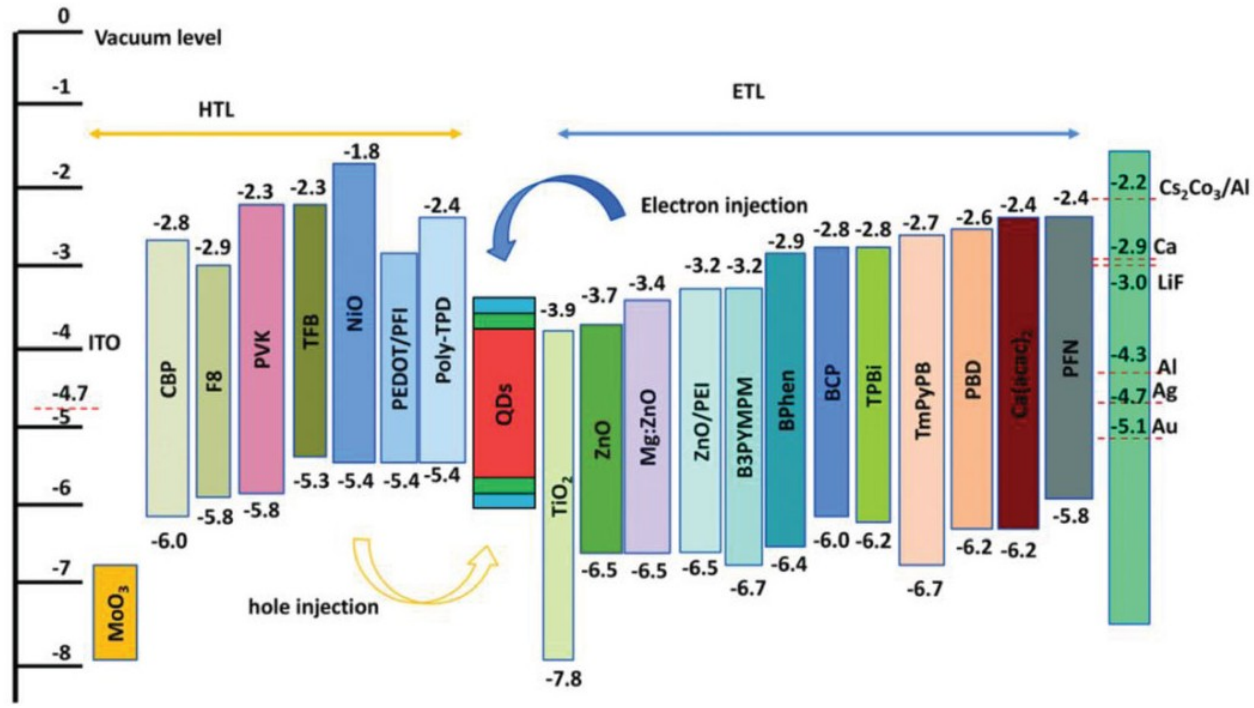


Figure 1.4. Energy levels of materials commonly used in the fabrication of QLEDs [27]

ETLs in QLEDs mostly utilize metal oxides, with ZnO nanoparticles being the most common owing to their high electron mobility, optical transparency, and favorable CB alignment. [28]. Furthermore, ZnMgO alloys have been developed to elevate the conduction-band minimum (CBM) and suppress excessive electron injection [28]. Alternatively, organic ETLs like (2,2′,2″-(1,3,5-benzinetriyl)tris(1-phenyl-1H-benzimidazole)) (TPBi) offer effective hole blocking but suffer from lower electron mobility.

Common organic HTLs in QLEDs include Poly[(9,9-dioctylfluorenyl-2,7-diyl)-co-(4,4'-(N-(4-sec-butylphenyl)diphenylamine)] (TFB), 4,4'-Bis(carbazol-9-yl)biphenyl (CBP) and 4,4',4-Tris(carbazol-9-yl)triphenylamine (TcTa), known for good hole mobility and suitable highest occupied molecular orbital (HOMO) levels that align with QDs. Also reported are Poly(9-vinylcarbazole) (PVK) and Poly[N,N'-bis(4-butylphenyl)-N,N'-bis(phenyl)-benzidine] (poly-TPD) as alternative HTLs in some QLED structures. In upright structures, Poly(3,4-ethylenedioxythiophene)-poly(styrenesulfonate) (PEDOT:PSS) is widely used as

the HIL, where for inverted Molybdenum(VI) Oxide (MoO_3) is commonly used. Even Phosphomolybdic Acid Hydrate (PMAH) can sometimes be used as an HIL alternative.

ITO is used as a transparent electrode because of its high transparency in the visible range, good conductivity, and compatibility with standard thin-film processing. Al or Ag are commonly used for the counter electrode because of their low work function. Al is easier to evaporate and widely used; Ag offers better reflectivity and sometimes lower contact resistance, but both often include thin interlayers (e.g., Lithium Fluoride (LiF)) to enhance charge injection.

1.2.3 Applications & Advantages:

QLED technology has advanced significantly in recent years, making it one of the most promising candidates for high-performance display and lighting applications. In commercial displays, QLEDs are utilized in both photoluminescent and electroluminescent modes. Photoluminescent QLEDs are widely integrated into Liquid Crystal Display (LCD) backlight units, where QDs serve as color converters to enhance color gamut and brightness, achieving over 90% Recommendation ITU-R BT.2020 (Rec. 2020) (international standard for ultra-high-definition (UHD) television color representation) coverage in high-end televisions [29, 30]. Electroluminescent QLEDs, on the other hand, employ QDs as active EMLs, offering precise color control, high luminance, and potential for flexible and transparent display architectures [29-31]. In addition to display technologies, QLEDs have been explored for solid-state lighting applications due to their high luminous efficacy, tunable correlated color temperature, and improved color rendering index, facilitating efficient and adaptable illuminating solutions [32].

The option of direct-write patterning without the need of masks or stamps can be provided by such technique as Electrohydrodynamic (EHD) jet printing [82]. By applying an electric field, droplets of QD inks are deposited onto substrates with high precision. While EHD

jet printing has the potential to achieve high resolution, issues such as nozzle clogging, ink instability, and environmental factors can lead to inconsistent droplet formation, impacting both resolution and yield [83].

In comparison to OLEDs, QLEDs exhibit numerous inherent advantages derived from their inorganic emissive materials. The inorganic nature of QDs enhances chemical, thermal, and environmental stability, reducing degradation from moisture and oxygen - factors that typically affect OLED performance and lifetime [33, 34]. Additionally, QLEDs have narrower FWHM emission peaks than OLEDs, which results in better color purity and more precise spectral control [35]. The solution-processable nature of QLED materials allows cost-effective fabrication through methods such as inkjet printing and spin coating, compatible with large-area and flexible substrates [33].

With the increasing use of smart devices, Flat Panel Displays (FPDs) have become ubiquitous with daily life in modern society. In FPD architectures, QLEDs are gradually explored as self-emissive pixels capable of replacing both backlight and color filter components, thereby simplifying device structure and improving optical efficiency. Unlike conventional LCDs that rely on transmissive light modulation, electroluminescent QLEDs emit light directly from each subpixel, enabling thinner form factors, wider viewing angles, and higher contrast ratios [7, 36]. Their compatibility with active-matrix driving schemes, particularly amorphous oxide and low-temperature polysilicon thin-film transistors (TFTs), enables simple incorporation into existing FPD manufacturing platforms [37]. Furthermore, the electrical stability and uniformity of QLED emission have demonstrated promising scaling for high-resolution displays, such as 8K televisions and microdisplays [38]. Ongoing optimization of charge transport layers (CTLs), barrier encapsulation, and QD surface passivation continues to improve operational stability and

luminance uniformity, reinforcing QLEDs as a strong contender for next-generation FPD technologies [32, 34].

1.3 RGB Patterning

RGB patterning, the process by which red (R), green (G) and blue (B) LEDs are formed side by side on the same substrate to form the subpixels (of a pixel) is an essential step in FPD manufacturing. In OLEDs, this process determines the spatial definition of each emissive subpixel, enabling full-color image formation through additive color mixing. Three main approaches have been developed to implement RGB pixel structures in OLEDs: (a) side-by-side RGB OLEDs, (b) white (W-) OLEDs combined with color filters (CFs), and (c) blue OLEDs coupled with color conversion media (CCMs), as shown in Figure 1.5 [39]. In the side-by-side RGB approach, individual R, G, and B OLED units are fabricated adjacent to one another within each pixel. This configuration offers the highest light utilization efficiency since emitted light is viewed directly without passing through filters. However, it requires precise shadow masking or multi-step deposition using fine metal masks (FMMs), which suffer from mask sagging, misalignment, and limited scalability to large-area substrates [40]. The W-OLED plus CF architecture simplifies fabrication by using a broadband white-emitting OLED layer with patterned RGB color filters deposited on top. Although this eliminates the need for multiple EMLs, CFs absorb a substantial portion of the emitted light (typically >60%), thereby reducing optical efficiency and accelerating device degradation due to higher required drive currents [41, 42]. The blue OLED (B-OLED) with CCM method employs a uniform layer beneath patterned R and G color conversion materials, which down-convert blue photons to longer wavelengths. This technique avoids multiple organic

depositions but faces challenges such as incomplete conversion and optical crosstalk between adjacent pixels [43].

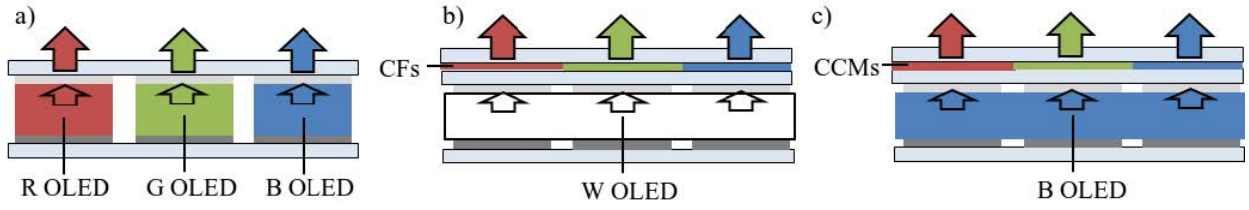


Figure 1.5. RGB approaches for OLED displays: a) side-by-side RGB OLEDs, b) white OLEDs plus CFs, and c) blue OLEDs with CCMs. [39]

To achieve fine RGB patterning suitable for high-resolution displays, several techniques have been investigated. Among them, FMM evaporation remains the most widely adopted commercial approach, although maintaining precise pattern definition becomes increasingly challenging as pixel density increases [44]. The use of this technique with QLEDs is however not feasible because QD materials can not be evaporated. Alternative strategies include inkjet printing, which enables additive deposition of emissive materials with sub-10 µm precision, and photolithography-based lift-off processes adapted for solution-processable emitters [45]. Recently, indirect photopatterning methods have been proposed, wherein EMLs are crosslinked into solvent-resistant networks prior to resist removal, allowing micro-scale RGB definition without exposing organic emitters to UV radiation or etchants [46].

1.4 Challenges in QLEDs

QLEDs have achieved significant progress in recent years, yet their practical implementation continues to be constrained by several material and process-related challenges that affect device efficiency, color uniformity, and long-term operational stability. Among these, challenges associated with ETLs, especially the widely used ZnO and ZnMgO systems, and the difficulties in producing uniform RGB patterning through inkjet printing have emerged as two of the most crucial factors.

1.4.1 ZnO/ZnMgO - Ubiquitousness and Limitations

Although ZnO and its alloy ZnMgO are widely employed as ETLs in QLEDs because of their suitable band alignment and high electron mobility, these oxide materials also exhibit electrical instability over time. Native point defects and surface adsorbates can alter their carrier concentration and interfacial energy levels, resulting in gradual variations in conductivity and device performance during operation or storage [47-49]. Consequently, while ZnMgO alloys can partially mitigate excessive electron injection by tuning the conduction-band position, long-term stability and reproducibility remain significant challenges, prompting ongoing research into improved ETL design and processing strategies.

1.4.2 RGB Patterning via Inkjet – Limitations

Inkjet printing has gained significant attention as a versatile method for patterning RGB in QLEDs due to its digital control, material efficiency, and compatibility with large-area and flexible substrates. As an additive, mask-free process, it offers clear advantages over traditional vacuum-based or photolithographic approaches for scalable display fabrication. Nonetheless, the technique still faces notable challenges in achieving high-resolution, uniform, and defect-free QD films. Variations in ink properties, substrate surface energy, and solvent drying behavior can result in non-uniform film morphology and reduced emission uniformity [50].

Despite recent progress in ink formulation and process control, consistent large-area printing with precise alignment and optical uniformity remains a key barrier to commercialization of inkjet-printed QLEDs.

1.5 Thesis Organization

The thesis is organized into six chapters. Chapter 1 provides an introduction, while Chapter 2 offers a literature review on the limitations in QLEDs related with ZnO/ZnMgO ETLs, followed by a discussion of RGB inkjet printing and its limitations, and concludes with an overview of alternative patterning techniques and their associated resolution and yield constraints. Chapter 3 outlines the objectives of the study and presents the methodology, including the materials, device configuration, and characterization techniques used. Chapters 4 and 5 present and discuss the experimental results of the thesis. Chapter 4 investigates the low efficiency in upright QLEDs with organic ETLs and explores strategies to overcome this limitation. Chapter 5 investigates a newly developed RGB patterning approach for inverted QLEDs. Finally, Chapter 6 summarizes the main findings of this work and offers recommendations for future research.

Chapter 2
Literature Review

While QLEDs have high color performance and brightness, their efficiency and long-term stability are greatly affected by the ETL properties and the quality of the QD EML interfaces. ETLs are critical components of QLEDs, controlling electron injection into the QDs-EML and contributing to overall charge balance within the device. Inorganic or metal oxides (MOs) such as ZnO and ZnMgO are widely employed due to their favorable band alignment and high electron mobility, while organic and hybrid ETLs offer alternative routes with differing fabrication and material characteristics. Despite their widespread use, each class of ETL presents intrinsic trade-offs that can influence device performance, including limitations in charge transport, interface compatibility, and reproducibility across devices.

In addition to material selection and charge transport considerations, another critical aspect of QLED fabrication is the patterning of RGB pixels, which determines display quality and reproducibility across devices. Various patterning approaches have been explored to deposit R-, G-, and B-QD layers, each offering trade-offs in resolution, process complexity, and scalability. While inkjet printing remains one of the most widely used methods due to its additive, mask free nature and compatibility with solution processed materials, alternative strategies such as photolithography, laser assisted transfer, and microcontact printing have also been investigated to address some other fabrication challenges.

This chapter begins with a detailed review of the most widely employed ETL materials, such as ZnO and ZnMgO, focusing on their electrical characteristics, defect-induced limitations, and aging behavior, followed by a discussion of alternative ETL materials. It then also investigates

RGB patterning techniques, discussing the constraints of inkjet printing and emerging approaches for higher-resolution pixel formation. Finally, the chapter synthesizes the main challenges associated with ETL optimization and RGB patterning, summarizing the critical limitations in device efficiency, stability, and pixel formation precision.

2.1 Electron Transport Layers in QLEDs

2.1.1 ZnO/ZnMgO ETLs

2.1.1.1 Electrical Properties and Defect Driven Transport

ZnO nanoparticles and Mg-doped ZnO (ZnMgO) layers are commonly used as ETLs in QLEDs because they provide relatively high electron conductivity, wide optical bandgaps, and CB alignment favorable for electron injection into typical QD-EMLs [28, 51]. Measurements and reports consistently show that the as-deposited ZnO (and ZnMgO) nanoparticle films contain high densities of surface and near-surface defects, most commonly oxygen vacancies (V_O) and zinc interstitials (Zn_i), which provide electronic states in the bandgap that act as charge traps [52, 53]. These trap states reduce radiative recombination in adjacent QD layers by providing non-radiative recombination pathways at the ETL/QD interface, and they therefore contribute to reduced EQE and photoluminescence (PL) quenching in devices where ZnO-based ETLs are used [52, 54].

2.1.1.2 Positive Aging Phenomena

Several studies have reported changes in ETL behavior with time - both during storage and under electrical stress, a phenomenon often referred to in QLEDs as “positive aging” (an increase of EQE or luminance over initial operation) or, conversely, as long-term degradation depending on materials and device architecture [55, 56]. Su et al. demonstrated that interfacial reactions between ZnMgO and Al cathodes can create interlayers (AlO_x) and alter oxygen vacancy populations, producing measurable increases in electron injection and EQE after shelf-

aging [55]. The underlying mechanisms involve a combination of factors, including redistribution or passivation of surface defects, formation of shallow donor states through oxygen-vacancy generation, and slight recrystallization of ZnO nanoparticles that improve carrier mobility and reduce trap density [49, 54]. In situ structural studies revealed that aging or mild bias stress can induce c-axis re-orientation in ZnO nanocrystals, accompanied by a measurable reduction in sub-gap absorption linked to defect passivation [49]. Although these changes improve efficiency temporarily, they also indicate that the oxide ETL remains chemically active, even after device fabrication. While positive aging may appear beneficial, its uncontrolled nature raises concerns for reproducibility and long-term reliability. The rate and extent of performance improvement vary strongly with storage conditions, air exposure, and cathode composition [57, 58]. Furthermore, once the beneficial interface rearrangement saturates, degradation processes such as interfacial oxidation or trap accumulation may dominate, causing eventual luminance decay [54].

2.1.1.3 Resistive Switching and Memristive Behavior

ZnO and ZnMgO ETLs are known to have resistive switching and memristive behavior, where the electrical resistance of the oxide changes reversibly under applied bias and shows a characteristic hysteresis in current-voltage (I-V) response. These phenomena primarily arise from the migration of mobile ionic defects, most notably oxygen vacancies, and the subsequent formation and rupture of conductive filaments within the oxide layer [59, 60]. Under an external electric field, oxygen vacancies drift toward the cathode, creating localized conductive paths that reduce the overall resistance. Reversing the bias polarity causes these filaments to dissolve or recombine with oxygen ions, restoring a high-resistance state. The dynamic redistribution of defects modifies local carrier concentration and barrier heights, resulting in time- and voltage-dependent conductivity and memory-like electrical characteristics. ZnMgO alloys show somewhat moderated switching because Mg incorporation alters defect formation energies and suppresses

excessive carrier accumulation, although vacancy migration and trap-mediated conduction can still occur under high electric fields [47, 61]. In QLEDs, such resistive switching and memristive behavior are detrimental because they disrupt the steady-state electron transport required for balanced charge injection and stable light emission. Ionic migration and field-induced defect motion within the ZnO or ZnMgO ETL lead to variations in local conductivity and interfacial potential, causing hysteresis in the device I-V characteristics, transient luminance fluctuations, and threshold voltage drift over time [47, 62]. These effects introduce variability among devices fabricated under similar conditions, reduce reproducibility, and complicate accurate performance assessment. In addition, the dynamic conductivity modulation disturbs electron-hole (e/h) balance, resulting in enhanced nonradiative recombination and exciton quenching at the ETL/QD interface [47]. Over prolonged operation, repeated bias cycling can induce permanent conductive filament formation, increasing leakage current and accelerating luminance degradation [47].

2.1.2 Alternative ETLs

Organic ETLs consist of conjugated small molecules or polymers that transport electrons via molecular orbitals rather than extended inorganic lattices like ZnO or ZnMgO [63]. Common small-molecule organic ETLs used in QLEDs include1,3,5-tris(1-phenyl-1H-benzimidazol-2-yl)benzene (TPBi), Bathophenanthroline (BPhen) and Tris(8-hydroxyquinoline)aluminum (Alq_3), while polymeric or ionic interfacial modifiers such as Polyethylenimine (PEI), Polyethylenimine ethoxylated (PEIE) and conjugated polyelectrolytes (for example PFN-Br) are widely used to modify cathode work function and interfacial energetics [64-66]. Organic ETLs are typically deposited at low temperature from solution or by thermal evaporation, enabling compatibility with flexible substrates and low thermal processing routes that are attractive for roll-to-roll manufacturing [67]. Organic ETLs also exhibit a wider latitude to defect density because charge

transport in these materials occurs mainly through hopping between localized molecular orbitals, making them less sensitive to structural or interfacial defects [68]. However, organic ETLs also have several limitations when compared with metal-oxide ETLs. Typical electron mobilities measured for organic ETLs like TPBi are orders of magnitude lower than those reported for metal oxides, which can increase series resistance and limit current driving at high luminance [63]. Organic interlayers such as PEI or PFN-Br are therefore often used in hybrid configurations (for example, PEI-modified ZnO or a thin TPBi layer atop ZnO) to combine the favorable conductivity of oxides with the interfacial control provided by organics [66, 69]. Moreover, organic materials are generally more susceptible to moisture and oxygen and can undergo morphological or chemical changes under prolonged electrical stress, which degrades device lifetime [70]. In addition, the less dense molecular packing and greater structural disorder in organic films can promote trap-assisted recombination and reduce reproducibility when scaling to large-area devices [63]. Conjugated polyelectrolytes and ionic modifiers (PFN-Br and PFN derivatives) may help in reducing interfacial traps and improving initial performance, but long-term chemical compatibility with QD surface ligands and cathode materials remains a recurring issue [65, 69]. However, inherently low electron mobility of these organic materials remains the key barrier to achieving high performance in QLEDs with organic ETLs.

2.2 Patterning Techniques in QLEDs

2.2.1 Inkjet Printing

To create full-color displays, QLED production requires fine patterning of R-, G- and B-QDs. Inkjet printing has emerged as the most commonly used patterning technique because of its mask-free, additive nature and ability to selectively deposit QD inks onto substrates.

2.2.1.1 Implementation

In QLED fabrication, inkjet printing is used to deposit colloidal QD inks onto prepared substrates, typically consisting of an anode, HTL, EML, ETL, and cathode [71, 72]. This process initially involves formulating a QD ink with controlled viscosity, surface tension, and solvent volatility, to enable stable droplet formation and precise deposition [72]. The ink is loaded into a drop-on-demand inkjet printhead, which deposits individual droplets onto the substrate in a specified pattern corresponding to R, G, or B subpixels [72]. Droplet volume, spacing, and deposition frequency are carefully managed to ensure uniform coverage and minimize defects. Following deposition, the printed films are subjected to post-treatment methods such as thermal or solvent vapor annealing in order to promote film coalescence, minimize pinholes and other morphological defects, and improve contact with the underlying ETLs or HTLs [72]. A schematic of the Inkjet Printing process is shown in Figure 2.1. The technique is fully additive and mask-free, allowing for precise control over pixel dimension and material placement. Proper substrate surface treatment, ink formulation, and drying conditions are essential for avoiding typical problems including coffee-ring development, uneven thickness, and droplet spreading, which can impair optical uniformity and device performance.

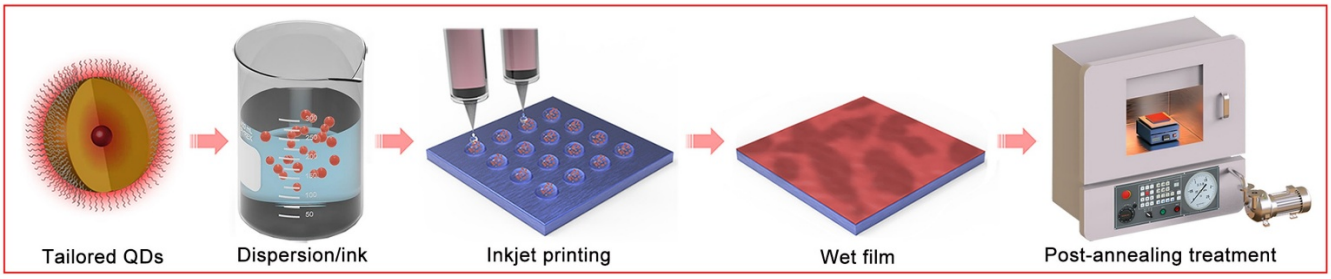


Figure 2.1. General schematic of the inkjet printing process in QLEDs. [73]

2.2.1.2 Limitations

A major challenge of inkjet printing is achieving uniform QD films due to complex droplet-drying dynamics. During droplet evaporation, capillary flows drive QDs toward the contact line leading to the well-known “coffee-ring” effect, where material accumulates at the droplet edge rather than uniformly across the display [74]. In QD-ink deposition, this edge accumulation results in variable film thickness, local refractive index changes, and spatial variation in emission intensity, thus compromising device uniformity, brightness, and color consistency [75]. Recent work shows that adjusting the ink's rheology (viscosity, surface tension), solvent-evaporation profile, substrate temperature, and surface energy can suppress this effect by shifting the flow regime from stick-slide or stick-jump toward uniform deposition, for example, by balancing capillary and Marangoni flows [76]. However, these adjustments introduce trade-offs: increasing viscosity or adding high-boiling-point solvents may stabilise drying yet reduce droplet ejection stability or degrade QD dispersion. Furthermore, printed droplets must not dissolve or damage underlying layers when they spread and evaporate on transport layers (like ZnO); in inkjet-printed QLEDs, the longer residence time and slower evaporation in comparison to spin coating increase the risk of intermixing and compromise layer integrity [77]. These effects get worse on large-area substrates by temperature gradients, nozzle drift, substrate motion, and uniformity in printhead droplet positioning, which lowers the yield and reproducibility of pixel morphology and device performance.

2.2.2 Other Patterning Techniques

Methods such as microcontact printing and capillary stamping utilize elastomeric stamps to transfer pre-patterned QD inks onto substrates [80, 81]. While suitable for flexible substrates and high throughput, stamp deformation, ink spreading, and misalignment can reduce pattern

fidelity, limiting the achievable resolution [80]. Variations in stamp wear and ink viscosity may introduce defects, further impacting yield [80].

Methods such as microcontact printing and capillary stamping utilize elastomeric stamps to transfer pre-patterned QD inks onto substrates [80, 81]. While suitable for flexible substrates and high throughput, stamp deformation, ink spreading, and misalignment can reduce pattern fidelity, limiting the achievable resolution [80]. Variations in stamp wear and ink viscosity may introduce defects, further impacting yield [80].

The option of direct-write patterning without the need of masks or stamps can be provided by such technique as Electrohydrodynamic (EHD) jet printing [82]. By applying an electric field, droplets of QD inks are deposited onto substrates with high precision. While EHD jet printing has the potential to achieve high resolution, issues such as nozzle clogging, ink instability, and environmental factors can lead to inconsistent droplet formation, impacting both resolution and yield [83].

Laser-induced forward transfer (LIFT) employs focused laser pulses to transfer QD materials onto substrates [84]. These methods can achieve high-resolution patterns and are suitable for selective deposition. However, thermal effects from the laser can cause damage to underlying layers or QDs, leading to performance degradation [85]. Additionally, the complexity of aligning the laser system and controlling energy delivery can affect reproducibility and yield.

Techniques like nanoimprint and microfluidic patterning use flexible molds or stamps to create patterns on substrates [86, 87]. These methods are cost-effective and can produce high-resolution features. However, issues such as mold wear, alignment precision, and material

compatibility can introduce defects, affecting both resolution and yield [86-88]. Furthermore, the scalability of these techniques to large-area production remains a concern.

2.2.3 Concept of RGB Patterning by Metal Quenching

An alternative approach for achieving color definition in QLEDs involves metal-induced quenching, where thin metallic layers are used to selectively suppress the emission from QD films. Previous work in our research group investigated the quenching phenomena of QDs by different metals and the influence of metal type and thickness on their optical and electrical properties. That work demonstrated that quenching by metals can define red, green, and blue emissive regions in QLEDs by selectively suppressing QD luminescence, taking advantage of the easy diffusion of vacuum-deposited metals into QD layers and the resulting Förster resonance energy transfer, which substantially reduces PLQY and EL [112]. The technique involves i) coating layers of QD materials with the desired luminescence colors, in sequence, without patterning using a suitable process (e.g. blade or spin coating) on the FPD substrate to form a stack, and ii) depositing a metal on a selected area of each QD layer after coating it (but before the next layer is coated) through a vacuum deposition process and a shadow mask for the purpose of substantially reducing their PLQY in the desired areas. As a result, when electrical bias is applied across the stack through a set of electrodes, the light that will be produced from the areas where the metal was deposited will be of a different color from that produced from the other areas as a result of some of the layers being quenched by the presence of the metals.

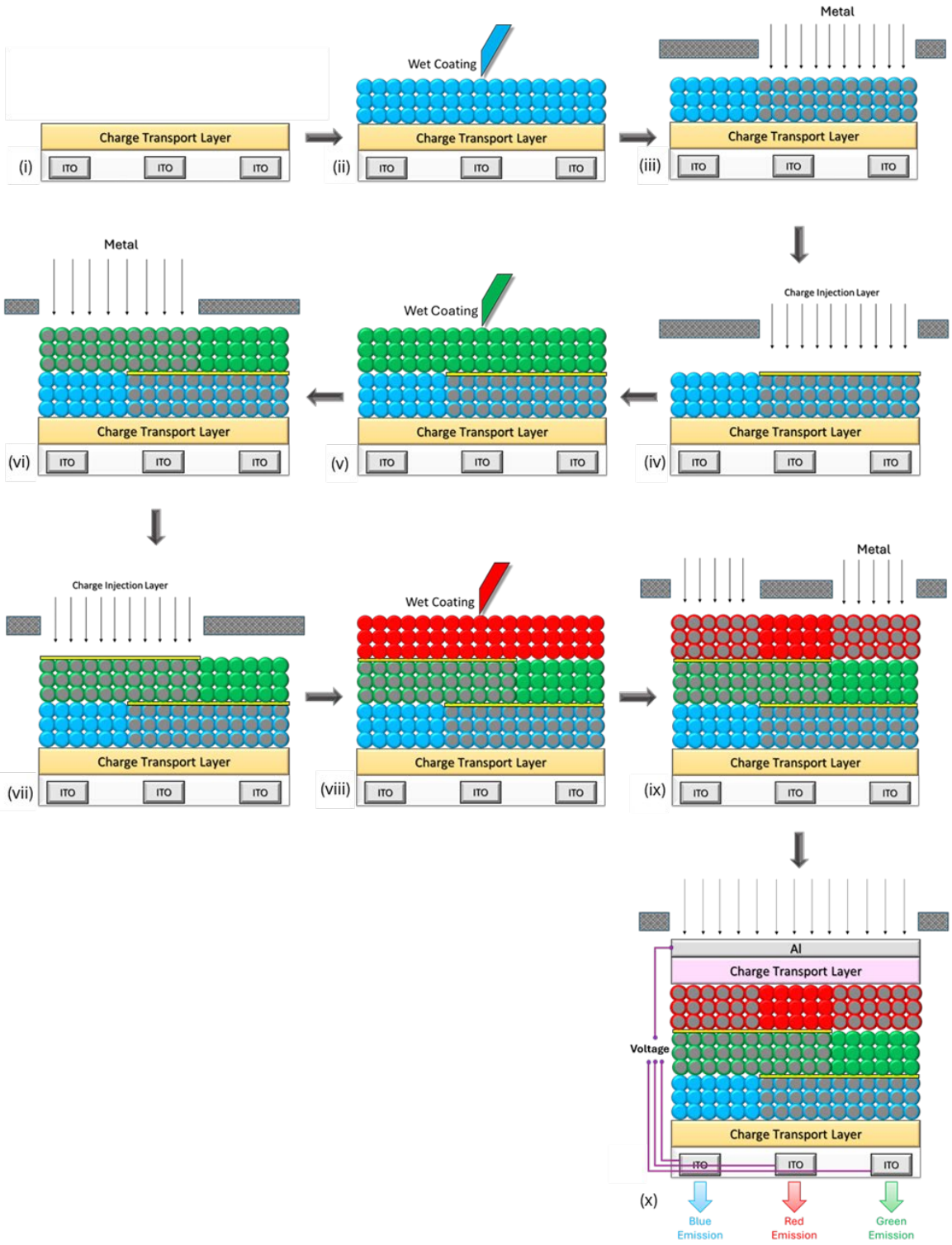


Figure 2.2. Schematic illustration of RGB color patterning in QLEDs, where sequentially deposited QD emissive layers are selectively quenched by vacuum-deposited metals in defined

areas, resulting in blue, green, and red emission from different areas of the stacked device under applied bias.

Figure 2.2 presents a schematic illustration of this technique, showing cross sectional views of the QD layers that are being coated, in sequence, one after the other, on the substrate, and the steps of depositing the quenching metal on a selected area of each of these layers after the layer is coated (but before coating the next one). Charge injection layers may also be deposited following the deposition of the quenching metal to assist with the injection of electrons or holes between layers, depending on the bias direction, as desired. In this figure, (i) a charge transport layer (CTL) is deposited onto an ITO-patterned glass substrate. (ii), (v), and (viii) depict the steps of coating layers of B, G and R QDs, in sequence, followed by the steps of respectively depositing the quenching metal (iii), (vi) and (ix) and a charge injection layer, (iv) and (vii), respectively, after each layer has been formed. The deposition of the quenching metal in steps (iii), (vi) and (ix) causes the PLQY of the QDs in each case to decrease in the treated area (illustrated by the change from the original color to grey in the treated areas in the respective figures). Figure 2.2 (x) illustrates the effect of applying an external bias across the top and bottom electrodes sandwiching the stack, and the emission of B, G or R EL from the different areas of the stack after the process has been completed. The use of metals as quenching agents also renders the quenched parts electrically conductive, making them capable of supplying charges to the other layers without significant ohmic losses.

2.3 Conclusion

In conclusion, QLED performance and stability is strongly influenced by ETL properties. While ZnO- and ZnMgO-based ETLs provide high electron mobility, they are susceptible to defect-induced charge trapping, aging effects, and resistive switching, which can limit efficiency, stability, and reproducibility. To address these challenges, organic ETLs can be considered as potential alternatives due to their favorable interfacial properties and low temperature processability. However, their relatively low electron mobility has traditionally been believed as the key factor limiting efficiency in QLEDs, as widely reported in the literature .

Furthermore, patterning in QLEDs remains a challenge that affects device resolution, color uniformity, and large-area manufacturability. Inkjet printing, while has a mask-free and scalable solution, often suffers from coffee-ring effects, droplet spreading, and non-uniform film deposition, which compromise pixel fidelity and yield. Alternative techniques such as photolithography, microcontact printing, electrohydrodynamic jet printing, laser-induced forward transfer, nanoimprint, and microfluidic patterning can achieve higher resolution, but issues related to process complexity, alignment precision, material compatibility, and scalability continue to limit their practical application. Thus, the development of a reliable, high-resolution, and scalable patterning approach remains essential for advancing QLED display performance and production efficiency.

Chapter 3
Research Objectives & Methodology

In this chapter, the research objectives are presented in Section 3.1, followed by the research rational described in Section 3.2. Finally, the research methodology and experimental details are explained in Section 3.3.

3.1 Research Objectives

3.1.1 Understanding and Overcoming the Poor Efficiency of QLEDs Utilizing Organic ETLs.

a. To investigate the effect of electron mobility of the organic ETL materials on device EQE.

b. To investigate if other possible factors are at play for the low efficiency QLEDs with organic ETLs

c. To develop and optimize ETL configurations that can improve charge confinement in the EML thus increasing EQE.

d. To investigate how the use of double and triple-layer organic ETL configurations with varying electron mobilities affects charge transport, recombination dynamics, and electron leakage behavior in QLED devices.

e. To achieve high-efficiency green and red QLEDs without using inorganic ZnO-based ETLs, demonstrating the potential of organic ETL architectures.

3.1.2 Testing the feasibility of RGB Color Patterning in QLED Panels via Quenching by Metals via a Shadow Mask.

a. To investigate the extent that metals deposited on the QD films can diffuse into them and effectively quench their PLQY.

b. To investigate the feasibility of using quenching by metals via a shadow mask for the purpose of color patterning to fabricate QLEDs that emit different colors.

c. To demonstrate the scalability of metal induced quenching for microscale pixel integration in QLED.

3.2 Research Methodology

3.2.1 Device Layout

Figure 3.1 presents a schematic illustration of the fabricated device layout, showing the coverage of the emissive and transport layers as well as the overlap between the ITO and metal electrodes that define the device area. The devices were fabricated on 50.8 mm × 50.8 mm glass substrates pre-patterned with 100 nm thick ITO electrodes having a sheet resistance of approximately 20 Ω/sq. Fourteen ITO stripes, each 2 mm wide, were patterned on opposite sides of the substrate to define one dimension of the active area. Near the substrate edges, the ITO pads were widened to 4 mm to ensure stable electrical contact during testing. On both sides of the ITO array, 7.4 mm wide ITO pads were used as counter electrodes and connected by a 100 nm thick Al layer, which defined the second dimension of the device. The overlap region between the bottom ITO and the top Al electrodes formed the active pixel area of 2 mm × 2 mm, within which the B-QD emissive and charge transport layers were sandwiched. A small rectangular marker on one of the ITO pads was used to indicate substrate orientation. To study multiple device structures on a single substrate, each substrate was divided into four sections, with each quarter containing three

ITO pads. Therefore, the data presented in this work were obtained from measurements performed on either six or twelve devices, depending on the configuration.

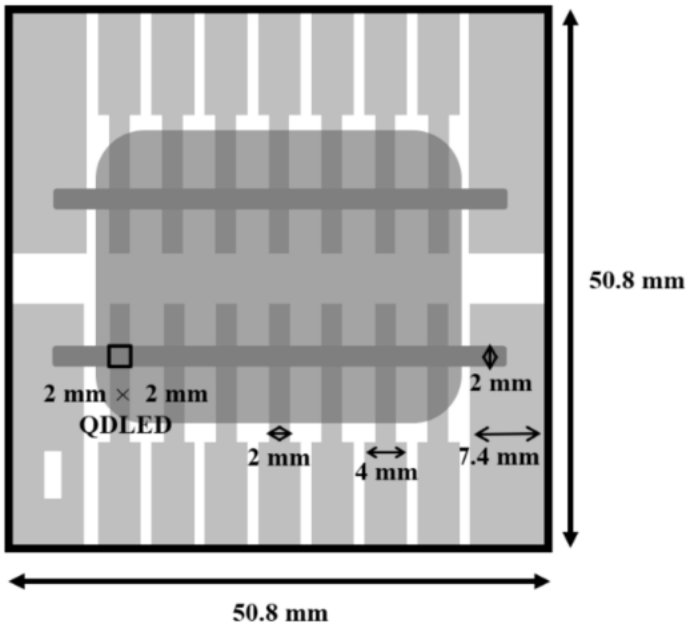


Figure 3.1. Schematic of the QLED substrate layout used in this study.

3.2.2 Device Fabrication

3.2.2.1 Inverted QLEDs

For inverted QLEDs, prepatterned indium tin oxide (ITO) coated on glass was used as a cathode. For device fabrication, the prepatterned ITO (100 nm) substrates were first washed with Micro 90, followed by a thorough cleaning process in an ultrasonic bath using deionized water, acetone, and isopropanol, respectively. After the substrates were cleaned, they were dried using nitrogen gas and then subjected to a 5 min treatment with oxygen plasma. Following this, a spin coating process was carried out using ZnO nanoparticles (30 mg/mL) dispersed in ethanol, at a speed of 3000 rpm for 60 s. The ZnO-coated layer was then subjected to annealing at 400 °C for 30 min. The QDs-EML (12.5 mg/mL) was spin-coated onto the ETL at 3000 rpm for 50 s, followed

by annealing at 70 °C for 20 min. R-QDs (PLQY = 90%), G-QDs (PLQY = 80%), dispersed in octane with the structure CdZnSe/CdZnS/ZnS were used as the EMLs. The hole transport layers (HTLs) CBP (40 nm) and Spiro-2CBP (20nm), the hole injection layer (HIL) MoO3 (5 nm), the electron transport layers (ETLs) 1,3,5-Tri[(3-pyridyl)-phen-3-yl]benzene (TmPyPB) (10nm) and TPBi (15nm), the electron injection layer (EIL) Mg (2nm), the anode Al (100 nm), and all the other metals (e.g. Ag and Au) were deposited using a thermal evaporation system (Angstrom Engineering) under a vacuum level of 5×10^{-6} Torr. For the blue OLED, a host : guest material system consisting of 2-tert-Butyl-9,10-di(naphth-2-yl)anthracene (TBADN) and 4,4'-Bis(9-ethyl-3-carbazovinylene)-1,1'-biphenyl (BCzVBi) were deposited using the same thermal evaporation system. For TFB, 8 mg/mL of solution was spin-coated at 3000 rpm for 40 s, followed by baking at 120 °C for 15 min.

3.2.2.2 Upright QLEDs

QLEDs with the upright architecture of ITO/PEDOT:PSS/TFB/QDs/ETL/LiF/Al, with ETL comprising single layer of Spiro-2CBP, 4,6-Bis(3,5-di(pyridin-3-yl)phenyl)-2-methylpyrimidine (B3PYMPM) and 4,6-Bis(3,5-di(pyridin-4-yl)phenyl)-2-phenylpyrimidine (B4PYPPM), double layer of B3PYMPM/B4PYPPM and triple layer of CBP/B3PYMPM/B4PYPPM are fabricated. To fabricate the devices, after washing with Micro 90, the prepatterned ITO (100 nm) cathode-coated substrates were cleaned in an ultrasonic bath with deionized water, acetone, and isopropanol, respectively. The substrates were then dried with nitrogen gas and treated with oxygen plasma for 5 min before the spin coating of PEDOT:PSS at 5000 rpm for 60 s. The coated PEDOT:PSS layer was baked at 150 °C for 15 minutes. Then the HTL layer or TFB (8 mg/mL) was spin-coated at 4000 rpm for 40 s, followed by baking at 120 °C for 15 min. The QDs-EML (12.5 mg/mL) dispersed in Octane was spin-coated on the HTL at 3000 rpm for 50 s and annealed at 70 °C for 20 minutes. Afterwards, CBP (5nm), along with the organic

ETLs (B3PYMPM and B4PYPPM), and the Electron Injection layer (EIL), LiF (1nm), and the Al (cathode) (100nm) sequentially deposited by thermal evaporation using a vacuum thermal evaporation system (Angstrom Engineering) under a base pressure of 5×10^{-6} Torr. The same recipes were followed in the fabrication of the single carrier devices. For the EODs, the ZnMgO NPs (30 mg/mL) dispersed in ethanol was spin coated at 3000 rpm for 40 s. The coated ZnMgO layer was then annealed at 100 °C for 15 minutes. Except for the PEDOT:PSS, all the solution-coating and annealing steps are performed under an N2 atmosphere in the glovebox.

The upright device structure was selected to ensure processing compatibility and interfacial stability when integrating organic ETLs with the QD-EML. In this configuration, the hole-side layers (PEDOT:PSS and TFB) can be solution-processed directly on the ITO anode under mild conditions, preventing their exposure to oxygen- or solvent-sensitive electron-transport materials. This sequence is particularly important because the organic ETLs used in this work, B3PYMPM and B4PYPPM, are not readily compatible with solution processing over QD films. These small-molecule materials are typically soluble only in chlorinated solvents such as chloroform or chlorobenzene, which can dissolve or damage the precoated QD layers, leading to morphological defects and loss of emission efficiency [96]. By employing an upright configuration, both ETL materials can be thermally evaporated on top of the QD layer, forming uniform layers without disturbing the underlying stack. This approach ensures reliable evaluation of electron injection and transport behavior while preserving QD film integrity. Furthermore, the upright structure yields chemically stable and well-defined QD/ETL interfaces that are free from the surface polarity and chemical reactivity often encountered with oxide-based ETLs [97]. Also, this configuration enables direct and quantifiable assessment of electron leakage, which is central to this study.

Finally, since the HTLs are deposited before the QD film, the architecture avoids potential solvent damage or interface disruption that would occur if these layers were processed on top of QDs.

3.2.3 Device Characterization

The J-V-L characterization of the QLEDs was conducted using an Agilent 4155C semiconductor parameter analyzer connected to a silicon photodiode and a Minolta Chroma Meter CS-100. The EL spectra were collected with an Ocean Optics QE65000 spectrometer. Transient photoluminescence (TrPL) measurements and PL measurements were conducted using an Edinburgh Instruments FL920 spectrometer. Shimadzu UV-2501PC spectrometer was used to collect the Transmittance spectra. Bruker FastScan/Icon® was used to conduct the AFM analysis. For the SEM analysis, Hitachi SU5000 FESEM was used. The TREL measurements were conducted using the same spectrometer with pulsed voltage applied from a Tektronix AFG3052C dual channel function generator.

3.2.4 Materials

Prepatterned ITO coated on glass substrates were purchased from Kinetic. CBP, TmPyPB, TPBi, B3PYMPM, B4PYPPM, TBADN and BCzVBi were purchased from Luminescence Technology Corp. R-, G-, and B-QDs, which are dispersed in octane with the structure Cadmium Zinc Selenide/ Cadmium Zinc Sulfide/ Zinc Sulfide (CdZnSe/CdZnS/ZnS) for R- and G- and Cadmium Zinc Selenide/Zinc Selenide Sulfide/Zinc Sulfide (CdZnSe/ZnSeS/ZnS) for B-QDs, were purchased from Mesolight Inc. ZnO NPs was purchased from SkySpring Nanomaterials, Inc. Au and Al were purchased from Angstrom Engineering. Ag and Mg were purchased from Materion. TFB was purchased from Xi'an Yuri Solar Co., Ltd. MoO3 was purchased from American Elements. All materials were used as purchased without modifications or further purification.

Among various types of QDs for light-emitting applications, such as InP, perovskite, and carbon-based QDs, CdSe QDs remain the most reliable and well-studied system for achieving high-performance QLEDs. InP QDs, although Cd-free and environmentally favorable, generally exhibit broader emission linewidths, lower PLQYs, and higher surface defect densities, which limit color purity and device efficiency [89, 90]. Perovskite QDs have good optical tunability but suffer from poor environmental and operational stability due to sensitivity to moisture, oxygen, and thermal stress [91]. Carbon and graphene QDs offer good chemical robustness but lack the precise bandgap control and high radiative efficiency needed for display-grade applications [92]. In contrast, CdSe QDs possess well-defined band structures and strong quantum confinement, allowing precise emission tunability with narrow linewidths below 30 nm and high PLQYs exceeding 90% [93, 94]. Their mature synthesis and well-established surface passivation strategies enable stable core/shell structures with low trap densities and efficient exciton confinement [11, 95]. In QLED architectures, their favorable energy-level alignment with CTLs such as ZnO, TFB, and CBP ensures balanced charge injection and reliable device operation.

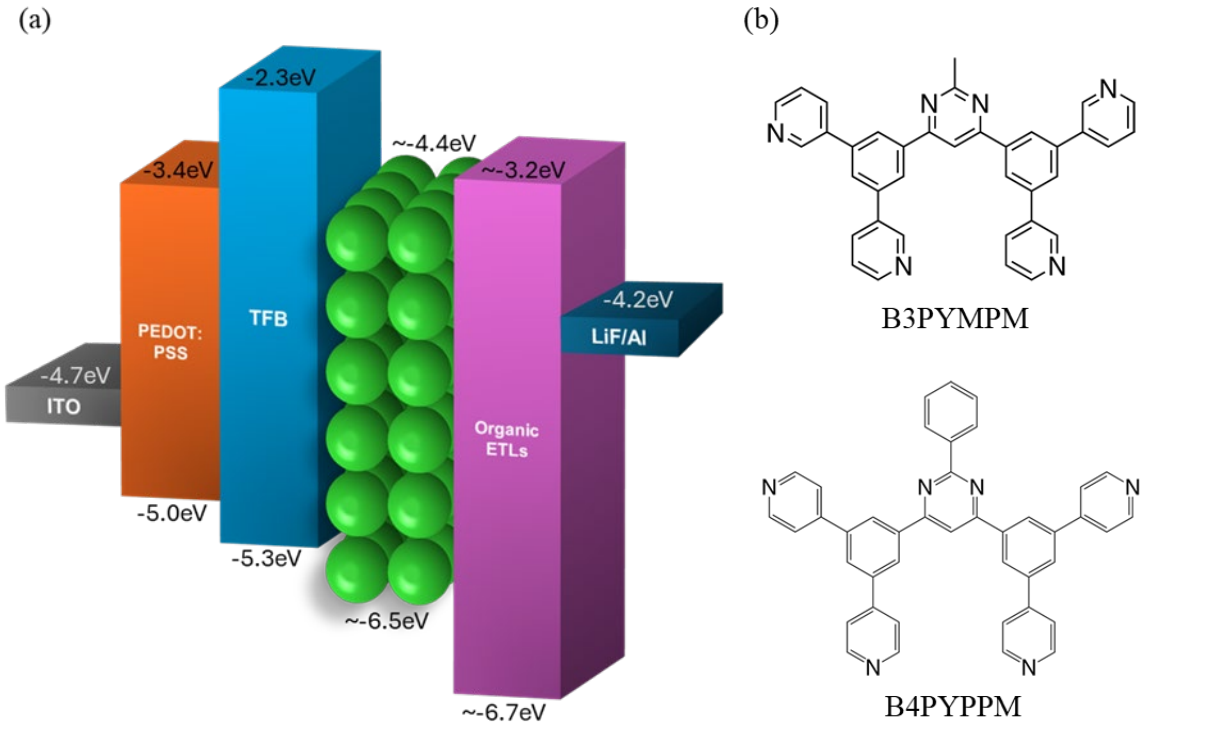
Chapter 4
Understanding and Overcoming the Poor Efficiency of QLEDs Utilizing Organic Electron Transport Layers

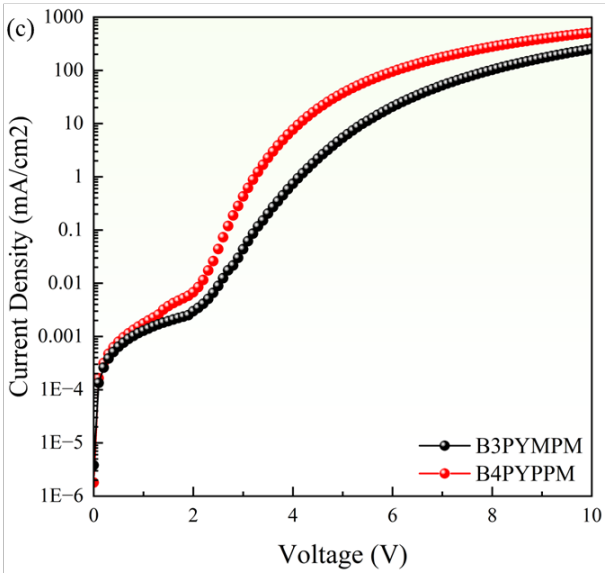
This part of the work was published as: *"Mobarak, B. S. B., and Aziz, H. "Understanding and Overcoming the Poor Efficiency of QLEDs Utilizing Organic Electron Transport Layers." Advanced Electronic Materials, 2025, e202500412"* and reproduced here. In this chapter, we test the use of organic ETLs in green QLEDs and investigate the factors that limit their efficiency. Comparative studies using two organic materials of different mobilities are conducted in order to understand the influence of ETL material electron mobility on device performance and determine if other factors are at play. Our findings show that, while the inherently low electron mobility of organic ETLs may play a role, the predominant factor behind the limited efficiency of these QLEDs is, surprisingly, the leakage of electrons from the QD EML to the HTL. By using a multilayer ETL configuration that includes electron blocking interfaces, electron leakage can be reduced, and higher EQE can be achieved. Through this approach a notable EQE of ~10% in green QLEDs that do not use ZnO ETLs has been demonstrated. The same ETL configuration is found to also realize EQEs of ~10% in red-emitting QLEDs indicating that the effectiveness of this approach is not limited to green QLEDs.

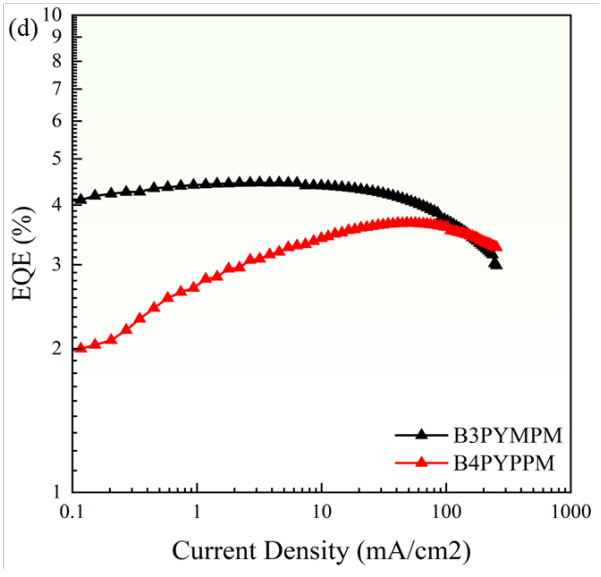
4.1 Results & Discussion

First, in order to investigate the effect of electron mobility of the organic ETL materials on device EQE, we fabricate and compare between the performance of green QLEDs in which two different materials with sufficiently different mobilities are used as ETLs. The devices

have a conventional upright architecture utilizing, ITO as anode, followed by a HIL of PEDOT:PSS, and a HTL of TFB. The EML comprises green QDs, followed by organic ETLs. LiF is used as the EIL, and Al serves as the cathode. The device structure, denoted as ITO/PEDOT:PSS/TFB/G-QDs/Organic ETLs/LiF/Al, is schematically depicted in Figure 4.1.a.







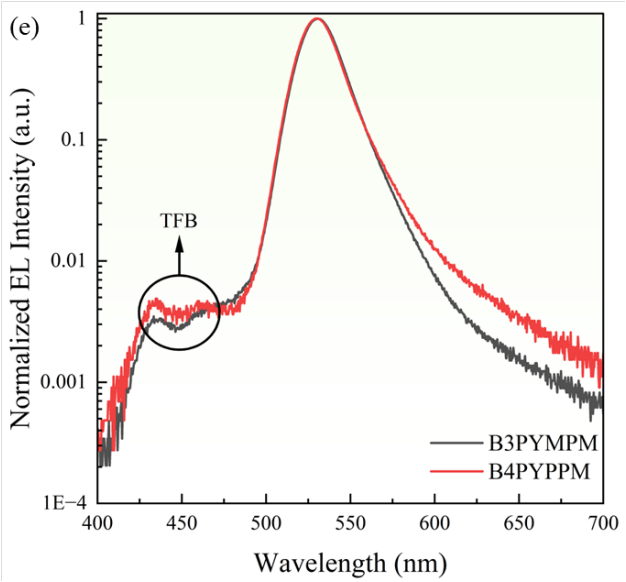


Figure 4.1. (a) A schematic diagram of the green QLED structure, (b) Molecular structures of the B3PYMPM & B4PYPPM, (c) J-V characteristics, (d) EQE vs J characteristics, and (e) Normalized EL spectra of QLEDs with the two different organic ETLs.

For ETLs, B3PYMPM and B4PYPPM are selected on account of their relatively high electron mobilities (~1.5 × 10^{-5} $cm^2/V{\cdot}s$ [98] and ~ 1.5 × 10^{-4} $cm^2/V{\cdot}s$ [99] , respectively) yet sufficiently different from each other to allow investigating the effect of mobility differences on device performance. The chemical structures of these two materials are shown in Figure 4.1.b. The high electron mobility of these materials is attributed to enhanced molecular stacking driven by intermolecular C-H···N hydrogen bonding interactions [98]. Additionally, due to the presence of pyrimidine groups, the materials have low-lying lowest unoccupied molecular orbital (LUMO) energy levels of around 3.2 eV and 3.26 eV respectively, which is close to the CBM of ZnO, indicating they may support efficient electron injection into the QD EML [99, 100]. The current density vs voltage (J-V) characteristics of devices with these two ETLs are shown in Figure 4.1.c. As can be seen, the devices exhibit comparable threshold voltages (V_{th}), indicating similar electron

injection properties which we attribute to the comparable LUMO levels of these organic ETLs thus also the electron injection barriers in the two cases. For all voltages above V_{th}, the device with the B4PYPPM ETL demonstrates a higher current density compared to the B3PYMPM ETL device as expected, consistent with the higher mobility and easier transport. Figure 4.1.d presents the EQE vs current density (J) characteristics of these devices. Surprisingly, despite its lower electron mobility, the B3PYMPM containing device exhibits a higher EQE for $J < 100$ mA/cm^2. This suggests that the lower electron mobility of the organic ETLs may not be the primary factor contributing to the reduced EQE in these devices. At higher current densities (i.e. for $J > 100$ mA/cm^2), the EQE gap diminishes, an observation that may be attributed to improved charge balance. The normalized EL spectra of the devices are shown in Figure 4.1.e. Both devices show almost identical green emission bands as expected. Interestingly, aside from the green emission band, the spectra also show a luminescence band around 450nm which corresponds to emission from the TFB HTL. The presence of this band points to some electron leakage into the HTL, resulting in electron-hole recombination within the layer. Such evidence of electron leakage into the HTL is surprising given the general assumption that the low efficiency of QLEDs with organic ETLs is caused primarily by poor electron supply (i.e. transport to and injection into) the QD EMLs.

Seeing that the lower electron mobility may not be the primary factor behind the low EQE in these devices and that some electron leakage to the HTL is occurring, we investigate the effect of using a B3PYMPM/B4PYPPM double ETL configuration instead of a single layer ETL, with B3PYMPM, the material with the lower mobility, placed next to the QD EML. In such configuration, one would expect a negative space charge to be formed at the interface between the

two organic materials [101] which would slow down the transport of electrons to the QD EML. Varying the thicknesses of each of the two layers while keeping their total thickness the same would allow changing the location of this space charge, thus electric field distribution, within the ETLs, thereby modulating electron transport.

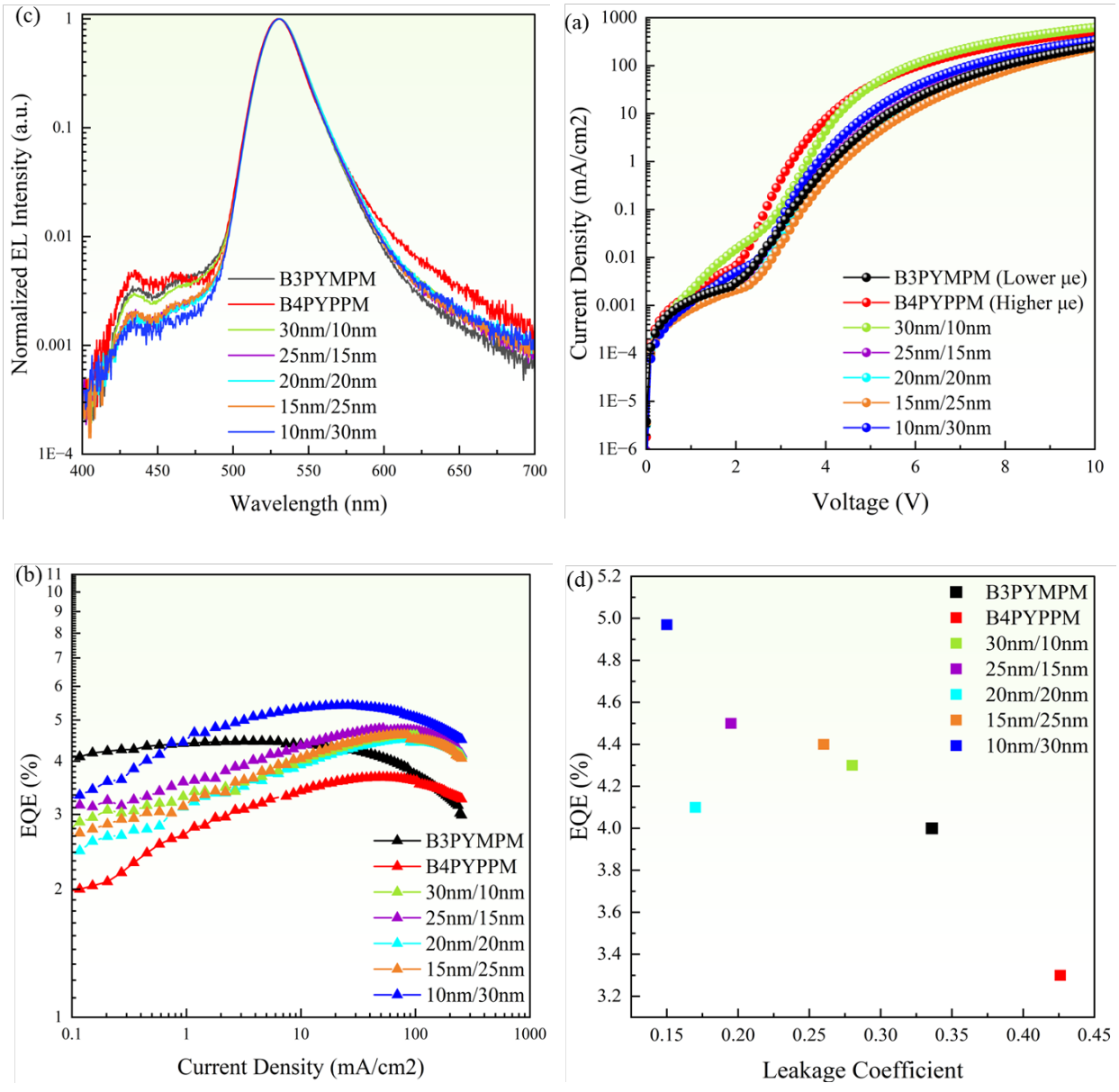


Figure 4.2. (a) J-V characteristics, (b) EQE vs J characteristics, (c) Normalized EL spectra, and (d) Leakage coefficient of devices with double ETLs of various layers thicknesses. Characteristics from the single layer are also included for comparison.

The double-layer organic ETLs device structure employed in this study is ITO/PEDOT:PSS/TFB/G-QDs/B3PYMPM(X nm)/B4PYPPM(40 – X nm)/LiF/Al. With a total overall thickness of 40nm, the double ETL configuration has the same thickness as in the single layer devices tested earlier. Devices with five different double-ETL thicknesses are fabricated and tested. Figure 4.2.a shows the J-V characteristics of these devices along with the characteristics from the single layer ETLs shown earlier for comparison. As seen from the figure, all double-ETL devices have V_{th} values similar to that of the single layer B3PYMPM device indicating that the V_{th} is primarily governed by electron injection at the QD EML/ETL interface. Also as seen, all the double ETL devices have lower currents at $V > V_{th}$ in comparison to the single layer B4PYPPM device, indicating that the presence of the B3PYMPM layer indeed slows down the electron transport. Despite this, they all show higher EQE values relative to the single layer B4PYPPM device again suggesting that a higher EQE is not correlated with easier or more efficient electron transport (Figure 4.2.b). Among these, the 10nm/30nm double ETL device gives the highest maximum EQE and the highest luminance at 20 mA/cm², approximately 5.4% and 4150 cd/m², respectively. In contrast, the single-layer B4PYPPM device yielded a max EQE of only 3.67% at the same current density. A summary of the EL measurement results for these devices is provided in Table 4.1:

Device	Operational Voltage (V)	Luminance (cd/m^2) @ $20mA/cm^2$	Max EQE(%)
B3PYMPM (40nm)	5.2	3500	4.45
B3PYMPM (40nm)	4.8	2900	3.67
B3PYMPM(30nm)/B4PYPPM(10nm)	4.9	3800	4.6
B3PYMPM(25nm)/B4PYPPM(15nm)	5.3	3700	4.74
B3PYMPM(20nm)/B4PYPPM(20nm)	5.5	3500	4.51
B3PYMPM(15nm)/B4PYPPM(25nm)	5.6	3900	4.63
B3PYMPM(10nm)/B4PYPPM(30nm)	5.2	4150	5.41

Table 4.1. Driving voltages, luminance at 20 mA/cm², and max EQE values for the investigated devices.

Figure 4.2.c shows the normalized EL spectra for all devices. The spectra reveal that electron leakage, indicated by emission from the TFB layer, is again present across all. Among them, the device with the double-ETL exhibits the lowest relative TFB emission, suggesting the least electron leakage, and correspondingly achieves the highest EQE. In contrast, the device with the 30nm/10nm double-ETL gives the highest relative TFB emission, almost comparable to that of the single layer B3PYMPM device, and the EQE was also remarkably comparable. Using the height ratio of the TFB/QD emission bands as an indicator for the relative magnitude of electron leakage among the devices, we plot, in Figure 4.2.d, the EQE values at 20 mA/cm^2 versus that ratio, the latter referred to as “leakage coefficient” for the various devices. As seen, the plot shows a clear trend where generally the lower the leakage coefficient in a device the higher its EQE. This

indicates that electron leakage may indeed be playing a leading role in the generally low EQE of QLEDs with organic ETLs. We also note the different profiles of the EQE vs J characteristics of these devices. So, while the B4PYPPM single layer device shows an EQE that increases with J, reaching a peak at around 80 mA/cm^2, the EQE of its counterpart with the B3PYMPM single layer remains relatively constant over the 0.1-80 mA/cm^2. The constant EQE suggests the electron-hole (e/h) ratio does not change appreciably with current over this range. Seen in contrast to the B4PYPPM single layer device, this suggests that the use of the lower electron mobility B3PYMPM ETL might be assisting hole injection into the QD EML, possibly due to a lower concentrations of electrons in the QD EML, which in turn causes electric fields across the layer to be higher, in turn assisting the cross over of holes across the HTL/QD EML interface. Turning the attention now to the double ETL devices, one can see that their EQE generally increases with J, reaching a peak at ~90 mA/cm^2 for all devices with the exception of the 10nm/30nm device where this peak is reached sooner (at ~20 mA/cm^2), resulting in a relatively flatter EQE over the 5-100 mA/cm^2 current range. This may again point to a scenario where electron and hole injection ratio remains relatively constant over a wider range of currents. That the 10nm/30nm configuration allows maintaining these optimal conditions over a wider current range in comparison to the other double ETL devices suggests that the distance between the organic/organic interface (hence the location of the negative space charge) and the QD EML or the HTL/QD EML interface plays a role in this behavior.

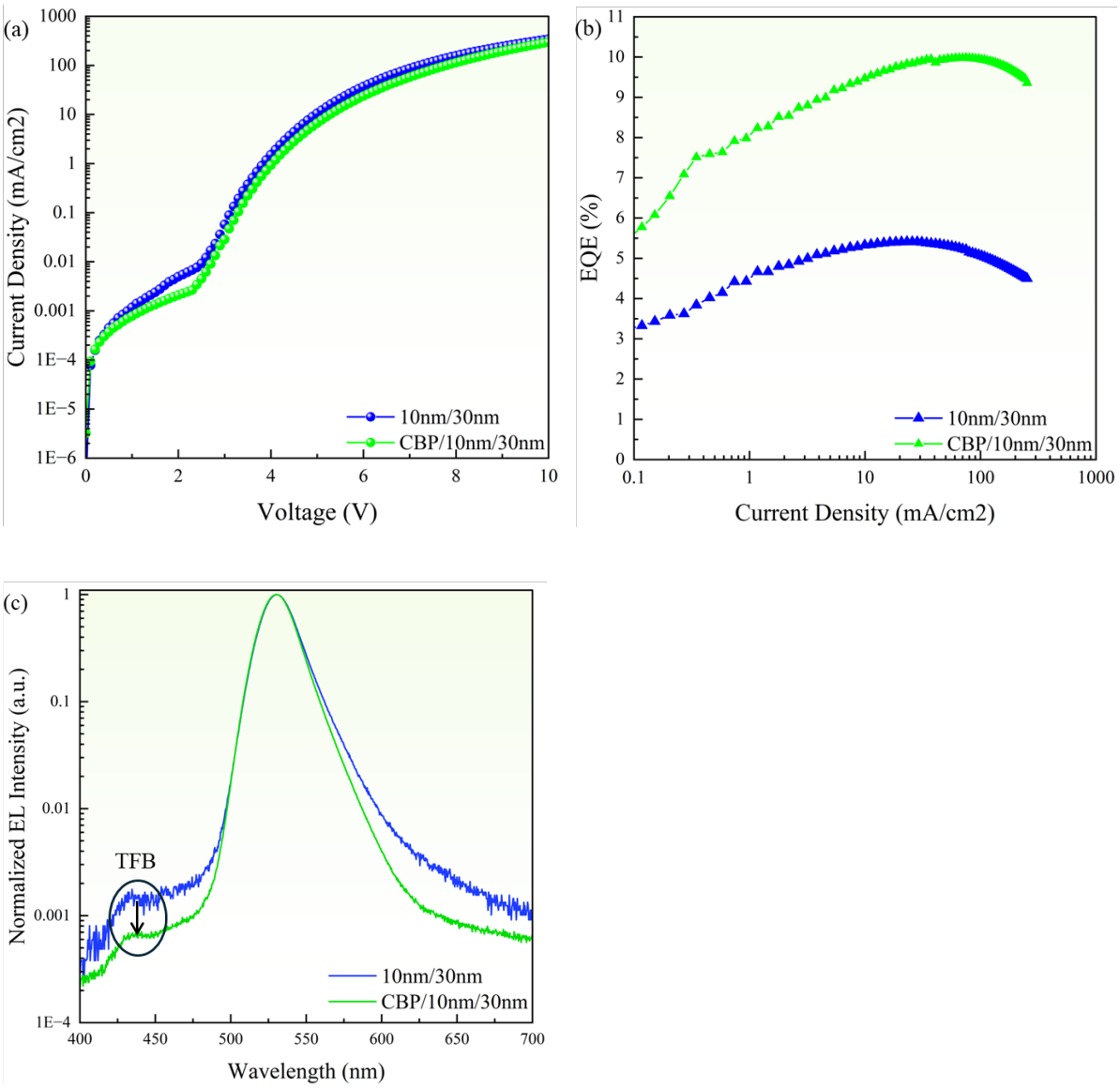


Figure 4.3. (a) J-V characteristics (b) EQE vs J, and (c) Normalized EL spectra of 10nm/30nm double ETL devices without and with the CBP layer.

Given the observations suggesting that a correlation exists between electron leakage into the HTL and variations in EQE, and the dependence of the extent leakage on the location of the negative space charge within the ETL we investigate the effect of using an additional (i.e. a third)

layer with a shallower LUMO that would create an additional organic/organic interface with electron blocking characteristics before the QD/ETL interface. For this purpose, we use a 5nm thick layer of CBP in between the B3PYMPM and the QD layers. With a LUMO of 2.9 eV [102], ~0.3eV shallower than B3PYMPM, one would expect the CBP/B3PYMPM interface to partially block electrons. Additionally, with a bandgap of ~3eV [102], one would expect CBP to help with hole and exciton confinement within the QD EML [103]. The purpose of this experiment is to provide additional verification if electron leakage is indeed the key factor limiting EQE in QLEDs utilizing organic ETLs and to assess whether its further suppression can lead to improved device performance. Figure 4.3.a depicts the J–V results from this device, with characteristics from the double-layer 10nm/30nm device also shown for comparison. The J–V characteristics are very similar in both cases with the device containing the CBP interlayer showing a slightly lower current density at any given voltage. This reduction can again be ascribed to the role of CBP layer in further slowing down the electron supply to the QD EML, further moderating electron transport. Despite this, the EQE vs J plot (Figure 4.3.b) shows that the device with the CBP interlayer has a maximum EQE of ~10%, almost 2X higher than its counterpart with the double ETL structure (only 5.4%), demonstrating a luminance of approximately 8200 cd/m² at 20 mA/cm^2, versus only 4150 cd/m² by its counterpart. To the best of our knowledge, the EQE reported in this work represents the highest value achieved for a green QLED that does not utilize a ZnO-based ETL. The normalized EL spectra (Figure 4.3.c) show a reduction in TFB emission in case of the CBP-containing device, signaling a significant reduction in electron leakage into the HTL. While the triple layer (CBP/10nm/30nm) ETLs slow down electron transport, resulting in a slight reduction in current density at any given voltage, this is offset by the significant improvement in EQE, driven by the reduced electron leakage and enhanced electron-hole recombination efficiency within the

QD layer. These observations highlight the strong connection between suppressing electron overflow, improved charge balance and overall device efficiency in these devices. Therefore, controlling electron leakage appears to be a key factor in achieving high EQE in QLEDs with organic ETLs.

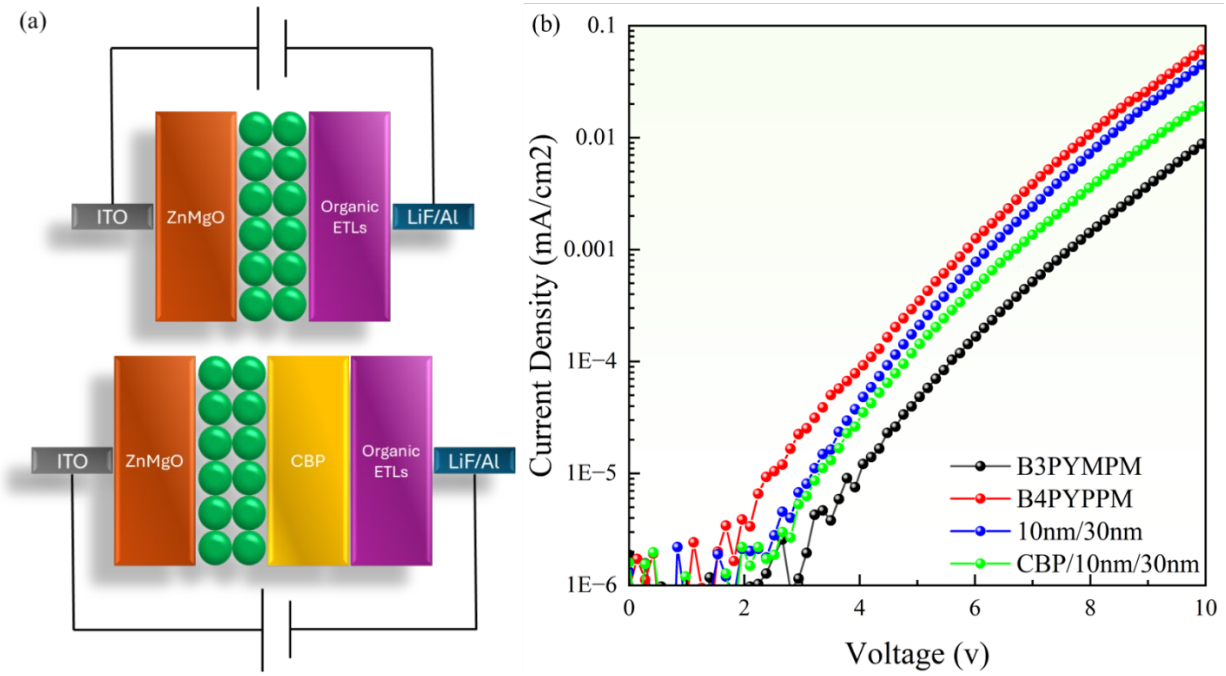


Figure 4.4. (a) Schematic diagrams showing the structures of the EODs with and without CBP, and (b) J-V characteristics of the same EODs.

In order to verify if the 10nm/30nm double ETL configuration as well as the triple layer ETLs indeed slow down the electron transport relative to the single layer ETLs as suggested from the J-V characteristics above, we test and compare these ETLs in electron only devices (EODs). EODs of the following structures were therefore fabricated and then their J-Vs compared: ITO/ZnMgO/G-QDs/ETL/LiF/Al with ETL = B3PYMPM (40nm), B4PYPPM (40nm),

B3PYMPM(10nm)/B4PYPPM(30nm) or CBP(5nm)/B3PYMPM(10nm)/B4PYPPM(30nm). Figure 4.4.b shows the J-V characteristics of these EODs. Under a forward bias, defined as LiF/Al contact being at a more negative potential relative to the ITO, electrons will be injected from the LiF/Al contact into the organic ETLs and subsequently into the QD layer to be eventually collected by the ITO contact through the Zinc Magnesium Oxide (ZnMgO) layer. In contrast, due to the hole blocking nature of ZnMgO and the ITO/ZnMgO interface, hole injection from the ITO contact under the same bias direction will be negligible. As can be seen, for the single layer ETLs, B4PYPPM exhibits a significantly higher current at any given forward bias voltage relative to the B3PYMPM consistent with the higher electron mobility. Also, the double layer and the triple layer ETL configurations give increasingly lower J at any given voltage relative to the single layer B4PYPPM EOD, verifying that the double and triple layer ETLs increasingly slow down electron transport as expected. These observations are in line with the progressive decrease in electron leakage evident in the decreased TFB band intensity, and the subsequent increase in EQE in QLEDs with these ETLs in the same order. Surprisingly however, the single layer B3PYMPM EOD shows a lower current than the double and triple ETL EODs, which was not expected given the relatively higher TFB emission and lower EQE that the QLED with the single layer B3PYMPM layer showed relative to its counterparts with the double and triple ETL counterparts (in Figure 4.3). This observation suggests that the suppression of electron leakage may not be exclusively due to the reduced electron currents. One possibility is that the presence of interfaces within the ETLs effectively leads to electron accumulation, causing a redistribution of electric fields within the QD EML and the HTL which promotes hole injection [104, 105]. As a result, e-h recombination efficiency within the QD EML is enhanced and electron leakage to the HTL reduced. The significantly lower current of the B3PYMPM single layer EOD also suggests that electron

injection at the B3PYMPM/Al interface may also be much less efficient than at the B4PYPPM/Al interface, indicating that the current difference between the two cases may not be entirely due to mobility differences.

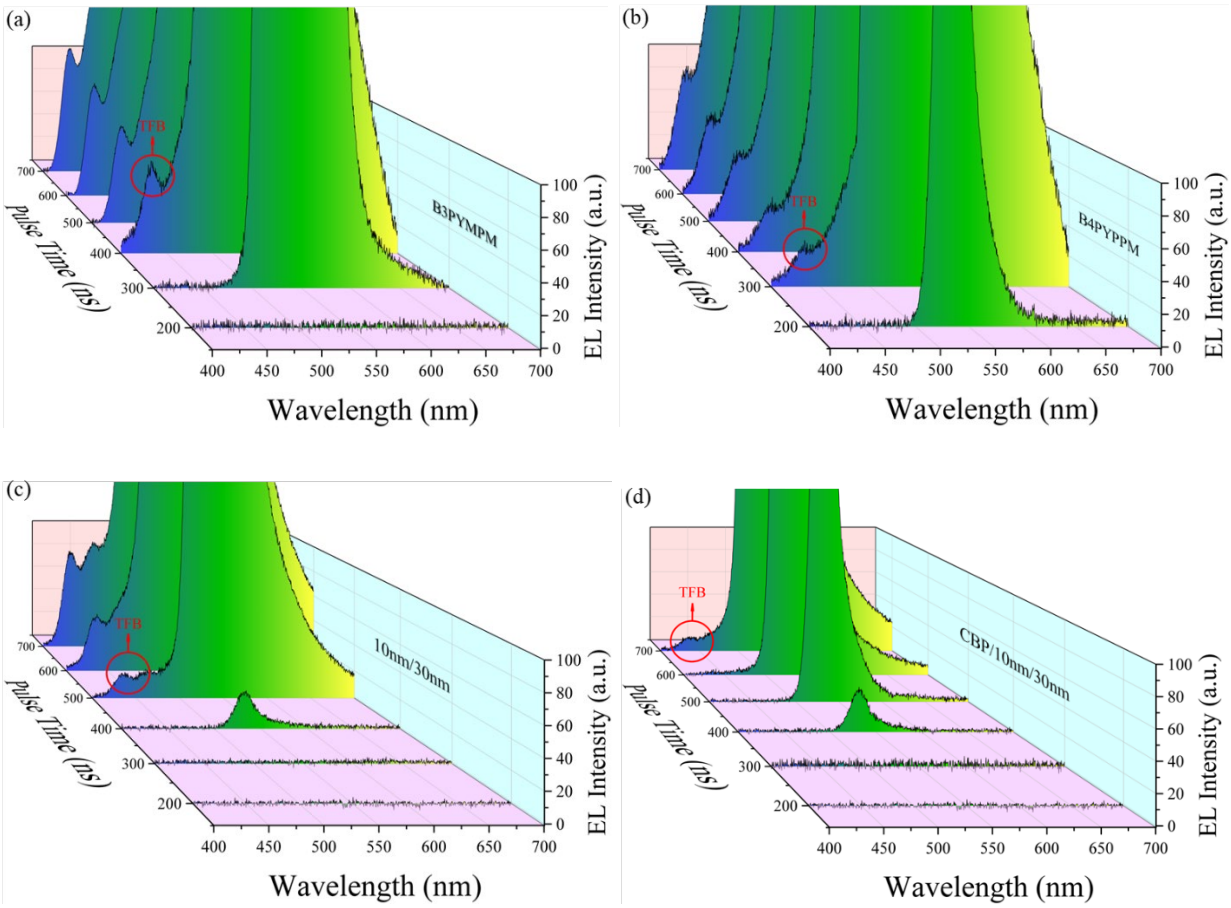


Figure 4.5. TREL spectra measured under pulsed current with varying pulse durations for the QLEDs with; (a) B3PYMPM single layer ETL, (b) B4PYMPM single layer ETL, (c) double layer (10nm/30nm) ETL, and (d) triple layer (CBP/10nm/30nm) ETL.

.

In order to further elucidate the functional role of CBP in regulating electron transport and reducing their leakage to the HTL, Transient Electroluminescence (TREL) measurements were conducted on QLEDs with single-layer B3PYMPM and B4PYPPM, the 10 nm/30 nm double-layer, and the triple-layer (CBP/10 nm/30 nm) ETL configurations. For these measurements, a square pulsed forward bias voltage with different pulse widths ranging from 200 to 700 ns, at a frequency of 1 MHz, and 50% duty cycle, is applied on these devices from a signal generator, and their EL spectra are collected. The magnitude of the forward bias voltage is adjusted for each device in order to ensure the EL spectra are collected from all devices at comparable current densities based on their J–V characteristics. Figure 5a–d shows the EL spectra and how they change with pulse widths, measured at 5, 3.9, 4.6, and 4.9 V for the single-layer B3PYMPM and B4PYPPM, the double, and the triple-layer ETL QLEDs, respectively. These voltages correspond to a current density of ~5.4 mA cm^{-2} in all devices. As seen, for all cases, the EL starts in the QD EML first and then starts to extend to the HTL as the pulse length increases. For instance, in the single-layer devices, QD emission begins at ~300 ns in the case of B3PYMPM and 200 ns in the case of B4PYPPM, with TFB emission not starting to appear until the pulse becomes ~100 ns longer in each case (i.e., at 400 and 300 ns, respectively (Figure 4.5.a and b). The earlier onset of TFB emission in case of the B4PYPPM ETL device can be attributed to its higher electron mobility compared to B3PYMPM, facilitating faster electron leakage to the HTL. For the double and triple-layer ETL devices (Figure 4.5c and d, respectively), TFB emission begins at an increasingly delayed onset of ~500 ns and 700 ns, respectively, suggesting that the ETL modifications indeed slow down the transport of electrons and their leakage to the HTLs, with the inclusion of the CBP layer further promoting this effect. The delay in TFB emission onset in case of the double and triple ETL QLEDs may be attributed to electron accumulation at the interfaces within these ETLs, leading to a redistribution of electric fields within the QD and the HTL which promotes hole injection as inferred earlier [104, 105]. Consequently, with increased hole injection and e-h recombination

within the QD EML, fewer electrons would leak to the HTL, therefore delaying the onset of TFB emission [54, 106].

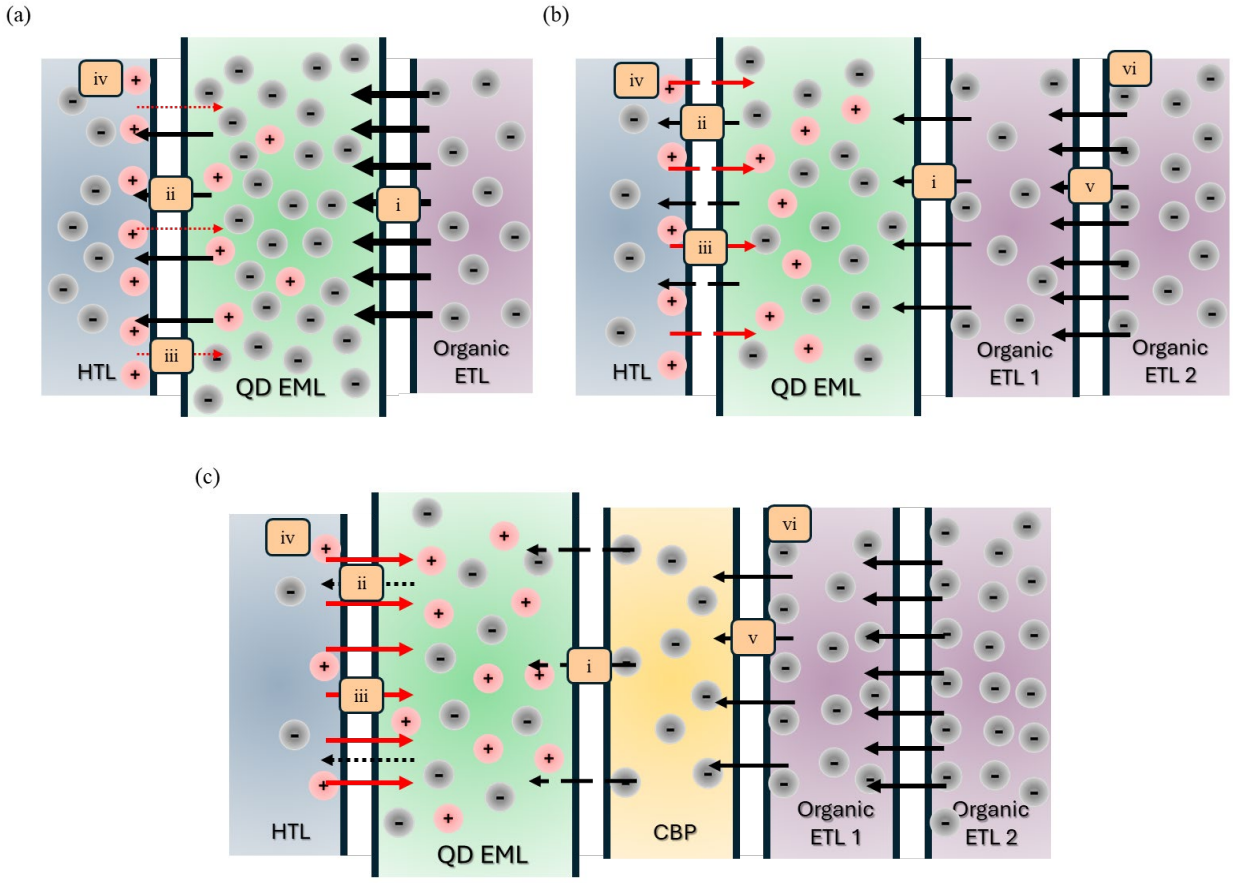


Figure 4.6. A graphical representation of a possible model for the reduced electron leakage and higher EQE of the devices with the double and triple ETLs depicting differences in charge injection and transport between the QLEDs containing (a) single layer, (b) double layer, and (c) triple layer ETLs. The numbers in the squares refer to the following processes or phenomena whereas the line width of the different arrows represent their relative magnitude where applicable [i] Electron supply to the QD EML, [ii] Electron leakage from QD EML to HTL, [iii] Hole injection at the

HTL/QD EML interface, [iv] Hole accumulation at the HTL/QD EML interface, [v] Electron injection between ETLs, and [vi] Electron accumulation at ETL interfaces.

Figure 4.6 shows a graphical representation that illustrates a possible model for the reduced electron leakage and higher EQE of the devices with the double and triple ETLs. On this figure, the labels i, ii ,iii, iv, v and vi correspond to the following injection or transport events or phenomena respectively; *[i] Electron supply to the QD EML, [ii] Electron leakage from QD EML to HTL, [iii] Hole injection at the HTL/QD EML interface, [iv] Hole accumulation at the HTL/QD EML interface, [v] Electron injection between ETLs, and [vi] Electron accumulation at ETL interfaces.* In the single-layer ETL device (Figure 4.6.a), the efficient injection of electrons from the cathode combined with their high mobility across the ETL leads to a high concentration of electrons across the ETL. As a result, electron supply to the QD EML [i] is high, resulting in a high concentration of electrons across the QD EML. A large fraction of these electrons leaks to the HTL [ii]. With more electrons reaching the HTL, fewer holes will be injected from the HTL to the QD-EML [iii], resulting in a larger number of holes accumulating at the HTL/QD EML interface [iv]. The high concentration of electrons across the QD EML will also reduce the electric field across the layer [107], which may also play a role in reducing hole injection at the HTL/QD EML [iii], contributing to hole accumulation [iv]. In contrast, in case of the double and triple ETL QLEDs (illustrated in figures 4.6.b and c respectively), the presence of additional interfaces will restrict electron injection between the ETL layers [v] resulting in electron accumulation [vi] and the formation of negative space charges that slow down charge conduction across the ETL. As a result, electron supply to the QD-EML [i] will be progressively less, leading to increasingly higher (i.e. more balanced) e/h ratios within the QD EML, hence the increasingly higher EQE of these devices,

respectively. With a smaller surplus of electrons within the QD EML, electron leakage to the HTL will also be less [ii]. With fewer electrons reaching the HTL, more holes will be injected into the QD-EML [iii], contributing to the higher EQE, and also reducing the number of holes accumulating at the HTL/QD EML interface [iv]. With a smaller surplus of electrons, hence a lower overall carrier concentration, in the QD EML of these devices, electric field across the layer will also be higher, possibly also assisting hole injection into the QD EML thus playing a role in reducing hole accumulation [iv].

We wish to also note that different from conventional QLEDs with ZnO ETLs, these QLEDs do not exhibit a positive aging effect [108]. comparative J-V-L measurements conducted on these devices over the first 72 hours after device fabrication show only a small decrease in current and luminance (Figure S1 and Table S1) The absence of positive aging behavior demonstrates one of the benefits of replacing ZnO with organic ETLs.

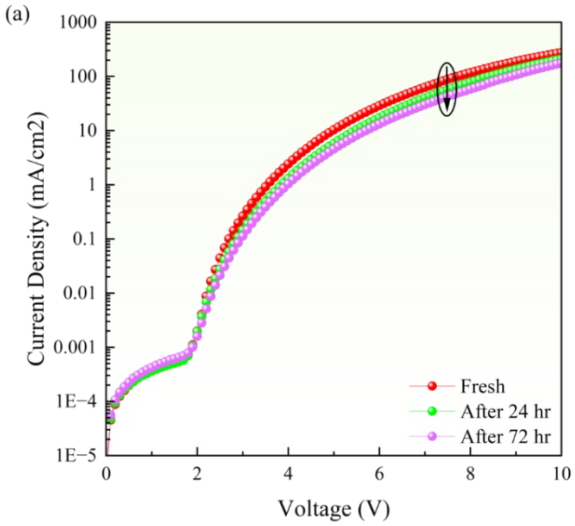


Figure 4.7. J-V measurements of the fabricated triple layer (CBP/10nm/30nm) organic ETLs structure done after 0 hour, 24 hours and 72 hours.

Time	Luminance (cd/m^2)
Fresh	8100
After 24 hours	7650
After 72 hours	6700

Table 4.2. Luminance values of the triple layer (CBP/10nm/30nm) organic ETLs structure measured after 0 hour, 24 hours and 72 hours

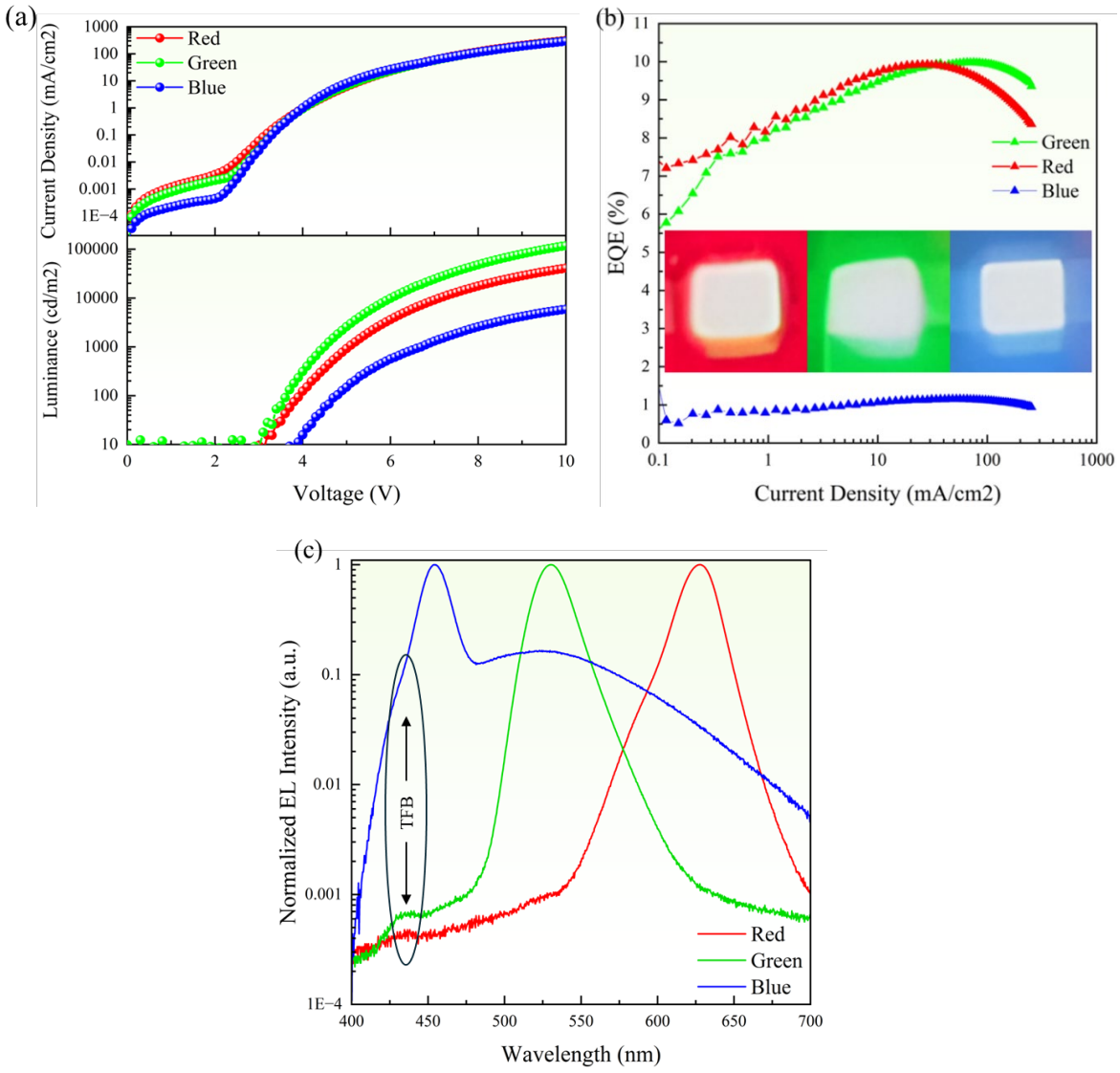


Figure 4.8. (a) J-V-L characteristics, (b) EQE vs J characteristics, and (c) Normalized EL spectra of the red, green and blue QLEDs with the organic ETLs.

Finally, we try the same triple-layer organic ETLs described above in red and blue QLEDs in order to test their suitability for QLEDs of different emission colors. We use the same device architecture as was used for the green QLEDs: ITO/PEDOT:PSS/TFB/R-QDs or B-QDs /CBP(5 nm)/B3PYMPM(10 nm)/B4PYPPM(30 nm)/LiF/Al. Figure 4.7 and table 4.2 shows the EL characteristics of these devices along with those of the green QLEDs presented earlier for comparison. The J-V-L characteristics of the devices (Figure 4.7.a) shows that all three devices exhibit comparable V_{th}, suggesting similar carrier injection and transport behavior. However, the blue QLED shows a higher turn-on voltage (V_{on}) compared to the red and green counterparts. This difference can be attributed to the larger hole injection barrier associated with the blue QDs, which hinders efficient charge injection and delays the onset of electroluminescence. At 20mA/cm^2, the red QLED gives a luminance of 3120 cd/m^2 and its EQE is on par with that of the green QLED (Figure 4.7b), demonstrating a maximum EQE of 9.9 %, and comparable to the highest reported for a red QLED with organic ETLs [109]. For the blue QLEDs, the luminance at 20 mA/cm2 in a group of 4 devices ranged between 300 and 410 cd/m2 and their maximum EQE between 1.1 - 1.86%. While these brightness levels are significantly lower than those displayed by their red and green counterparts, they are among the highest reported for blue QLEDs with organic ETLs [110]. The EL spectra, shown in Figure 4.3.c show no detectable emission from TFB in case of the red QLEDs, suggesting no significant electron leakage occurs. In contrast, some TFB emission is observed in case of the B-QLED spectrum, visible in the broad band in the 500-650 nm since in

this case the TFB 430 nm becomes harder to resolve due to its proximity to the B-QDs band. Such emission can be attributed to the familiar electron overflow phenomenon in blue QLEDs and suggests that a significant number of electrons still leak to the HTL in this case. [111]. The limited performance of the blue QLED, along with the observed TFB emission, suggests that further optimization is necessary. This may involve exploring alternative ETL materials, modifying the energy level alignment, or improving electron-hole recombination efficiency in the emissive layer. With continued refinement, it is anticipated that the EQE of blue QLEDs can also be significantly enhanced through the incorporation of suitable organic ETLs. Table 4.3 summarizes the main comparative EL parameters for the red, green, and blue QLEDs:

Device	**Operational Voltage (V)**	**Luminance (cd/m2) @ 20mA/cm^2**	**MAX EQE(%)**
Red	5.7	3120	9.9
Green	6	8150	10
Blue	5.4	300-410	1.1-1.86

Table 4.3. Measured performance parameters of Red, Green, and Blue QLEDs with organic ETLs.

4.2 Conclusion

In summary, this chapter investigates the root causes of the lower efficiency of QLEDs utilizing organic ETLs and approaches to mitigate them. While low electron mobility has traditionally been considered the primary constraint of organic ETLs, our findings reveal that

uncontrolled electron leakage toward the HTL plays a more critical role in limiting device performance. By using a multilayer ETL configuration that includes electron blocking interfaces, electron leakage can be reduced, and higher EQE can be achieved. Results from tests on EOD as well as TREL measurements reveal that minimizing electron leakage does not inherently correlate with reduced electron currents, suggesting a mechanism where the formation of electron space charges at interfaces in the organic ETLs and subsequent changes in electric field distributions may be assisting hole injection at the HTL/QD EML interface thus playing a role in the higher efficiency and reduced electron leakage. Using a triple layer organic ETL configuration made of CBP/B3PYMPM/B4PYPPM a notable EQE of 10%, the highest reported for a green QLED not utilizing ZnO has been demonstrated. The same ETL configuration is found to also realize EQEs of 9.9% in red-emitting QLEDs indicating that the effectiveness of this approach is not limited to green QLEDs. Collectively, these insights highlight the importance of layer interface engineering and leakage modulation over mere material mobility enhancement. The findings not only present a new approach for optimizing organic ETLs in QLEDs but also open up opportunities for the use of these modified layers as a replacement for ZnO hence mitigating some of the stability issues they impart on QLEDs. Future device architectures should prioritize interfacial control and charge confinement strategies to fully unlock the potential of organic ETL-based QLEDs in next-generation display and lighting technologies.

Chapter 5

Testing the Feasibility of RGB Color Patterning in QLED Panels via Quenching by Metals via the Use of a Shadow Mask

In this chapter, we introduce and investigate a novel approach for achieving RGB color patterning in QLEDs through selective quenching of QDs luminescence by metals, taking advantage of the ability of vacuum-deposited metals to diffuse easily through QD layers and to effectively quench their luminescence by energy transfer via the Forster resonance process, causing their photoluminescence quantum yield (PLQY) to be substantially decreased thus suppressing EL [112]. As discussed earlier in chapter 2, the technique involves i) coating layers of QD materials with the desired luminescence colors, in sequence, without patterning using a suitable process (e.g. blade or spin coating) on the FPD substrate to form a stack, and ii) depositing a metal on a selected area of each QD layer after coating it (but before the next layer is coated) through a vacuum deposition process and a shadow mask for the purpose of substantially reducing their PLQY in the desired areas. As a result, when electrical bias is applied across the stack through a set of electrodes, the light that will be produced from the areas where the metal was deposited will be of a different color from that produced from the other areas as a result of some of the layers being quenched by the presence of the metals. The use of metals as quenching agents also renders the quenched parts electrically conductive, making them capable of supplying charges to the other layers without significant ohmic losses. Because the metal deposition is done by vacuum deposition through a shadow mask (the same technology currently used in OLED FPD manufacturing), it can readily achieve the desired small feature sizes.

5.1 Results & Discussion

To begin, we first investigate the extent that metals can effectively quench the PLQY of QDs. Such quenching primarily occurs through Förster resonance energy transfer (FRET), in which the excited-state energy of a QD is non-radiatively transferred to a nearby acceptor - in this case, the metal - within a distance comparable to the Förster radius 'r' [112]. The transferred energy is then dissipated through non-radiative processes in the metal, resulting in a significant reduction of the QD PLQY, as schematically illustrated in Figure 5.1.a [113]. For this, we compare the PL spectra of R-QDs deposited on bare glass substrates with those of R-QDs coated underneath a thin Ag layer (1nm). Figure 5.1.b shows the PL spectra collected from these samples. The Glass/R-QDs/Ag film is significantly reduced (almost two orders of magnitude lower) compared to the Glass/R-QDs film. Consistently, the transient photoluminescence (TrPL) measurements (Figure 5.1.c) show a significantly shorter decay lifetime for Glass/R-QDs/Ag compared to Glass/R-QDs, indicating suppression of the radiative recombination pathway in the presence of the metal. The faster decay suggests the introduction of an additional non-radiative channel, consistent with energy transfer from the excited QDs to the metal surface where the excitation energy is dissipated. The combined steady-state and time-resolved data confirm that the presence of the metal leads to efficient non-radiative energy dissipation and thus verifies the capability of metals to quench QD luminescence. We therefore attribute such almost complete quenching to a possible diffusion of the metals into the respective QD layers, facilitating and enhancing non-radiative energy transfer from the QDs to the metals.

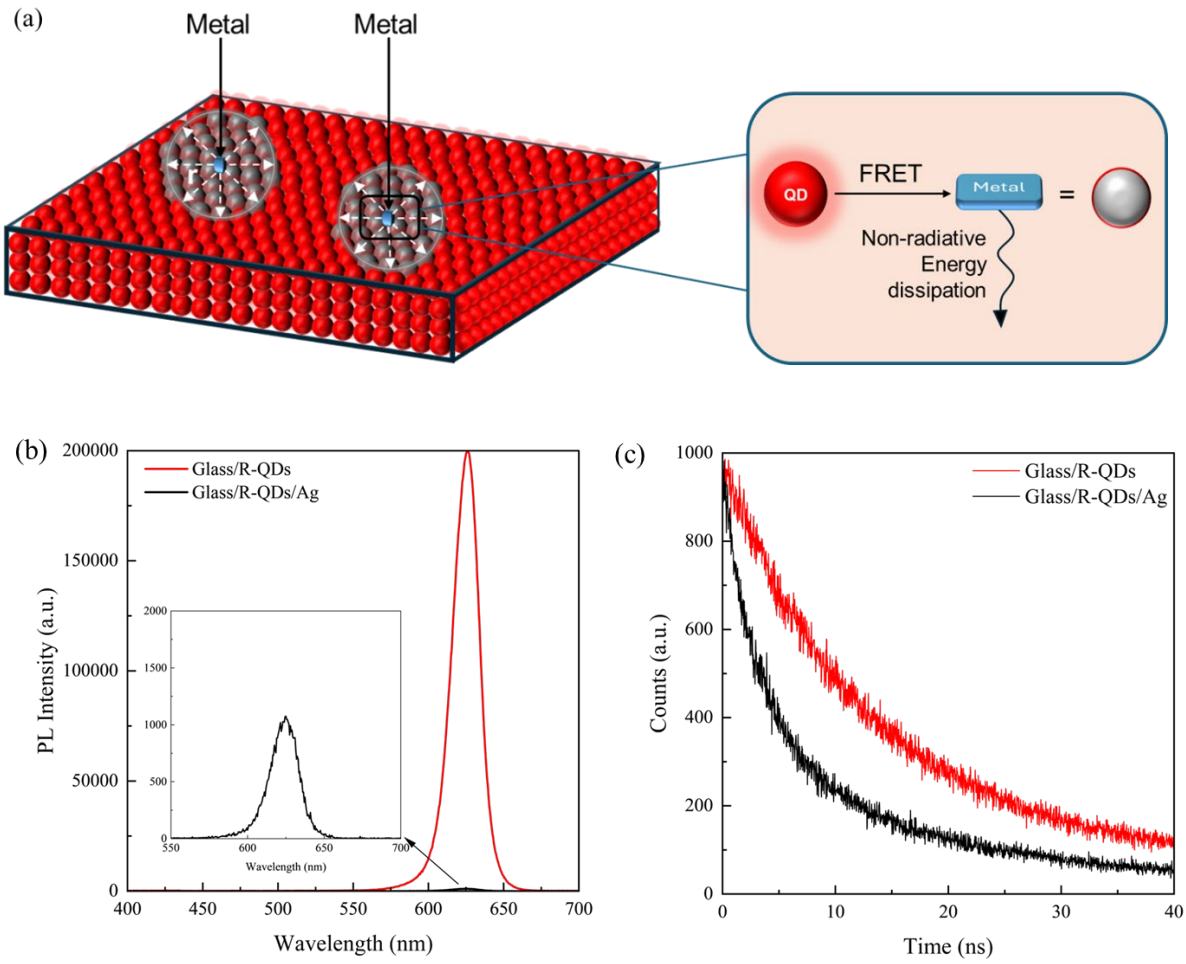


Figure 5.1. (a) Graphical representation of metal-induced QD quenching, (b) PL spectra, and (c) TrPL decay characteristics of Glass/R-QDs and Glass/R-QDs/Ag films under 365 nm excitation

In order to test if the metal may indeed be diffusing into the QD layers, we study and compare the optical properties and morphology of test samples of Ag films despoiled on glass substrates precoated with QD layers (i.e. Glass/R-QDs/Ag) against ones without the QD layers (i.e. Glass/Ag). Figure 5.2 shows the optical transmittance spectra collected from these samples. As seen, the Glass/Ag spectrum shows a typical spectrum for an Ag thin film showing a transmittance peak around 350nm which corresponds to the onset of interband electronic

transitions in Ag (electrons excited from the 4d band into the 5s/5p conduction band) [114] and limited transmittance in the 500-800nm range, arising from the reflective nature of the film. The Glass/QD/Ag, in contrast, shows lower transmittance in the 350-450nm range, due to absorption by the QDs [115, 116] yet higher transmittance otherwise, indicating Ag film is less reflective. This indicates that the Ag film that is coated on the QD layer must be thinner than its counterpart that is coated on the glass, suggesting that the metal must be penetrating into the QD layer.

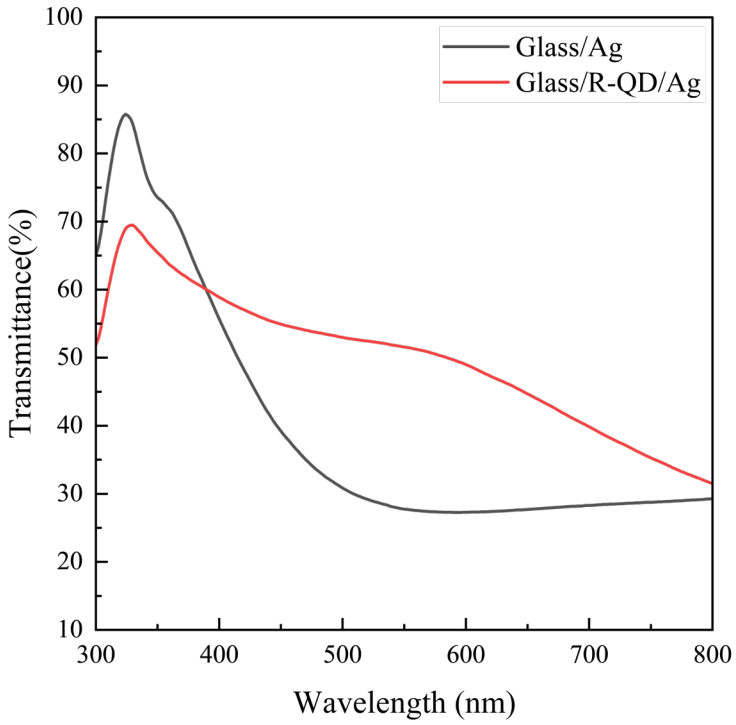


Figure 5.2. Transmittance analysis of the Glass/Ag and the Glass/R-QDs/Ag films.

To verify the phenomenon further, we also study and compare the surface topology of the metal films using Atomic Force Microscopy (AFM) and Scanning Electron Microscopy (SEM). Figure 5.3 shows top view images (a and b) and 3D images (c and d) of the

AFM surface scans from the Glass/Ag and Glass/R-QDs/Ag samples, respectively. As can be seen, the surface roughness of the Ag film is significantly higher when the QD layer is present, giving an RMS (surface roughness value) of 8.15nm versus only 1.75 nm in case of the Glass/Ag sample. The height difference between the highest and the lowest point of the surface measures 62 nm versus 12.2 nm in the two cases respectively. The high surface roughness, several times thicker than the thickness of the Ag on the QDs does not form a continuous film, consistent with the higher optical transmittance. The scans also show the presence of some features in certain areas with significantly elevated topography (10-20 nm higher than the rest, the lighter colored features) suggesting some metal island formation on the QD surface. The same features can also be seen on SEM images (Figure 5.3.f), where they again appear with higher contrast than the background, suggesting they are more e-rich thus more conductive relative to the background, consistent with them being Ag metal islands. Also, and again different from the Glass/Ag sample (Figure 5.3.e) where the SEM image shows a relatively uniform and featureless surface, the image from the Glass/R-QDs/Ag sample also shows some valleys and voids manifesting as dark features [117, 118]. Collectively, the much higher surface roughness coupled with evidence of only partial coverage by the metal, and the higher optical transmittance are consistent with a scenario where a significant fraction of the deposited Ag atoms may readily penetrate into the QD film instead of staying on the surface.

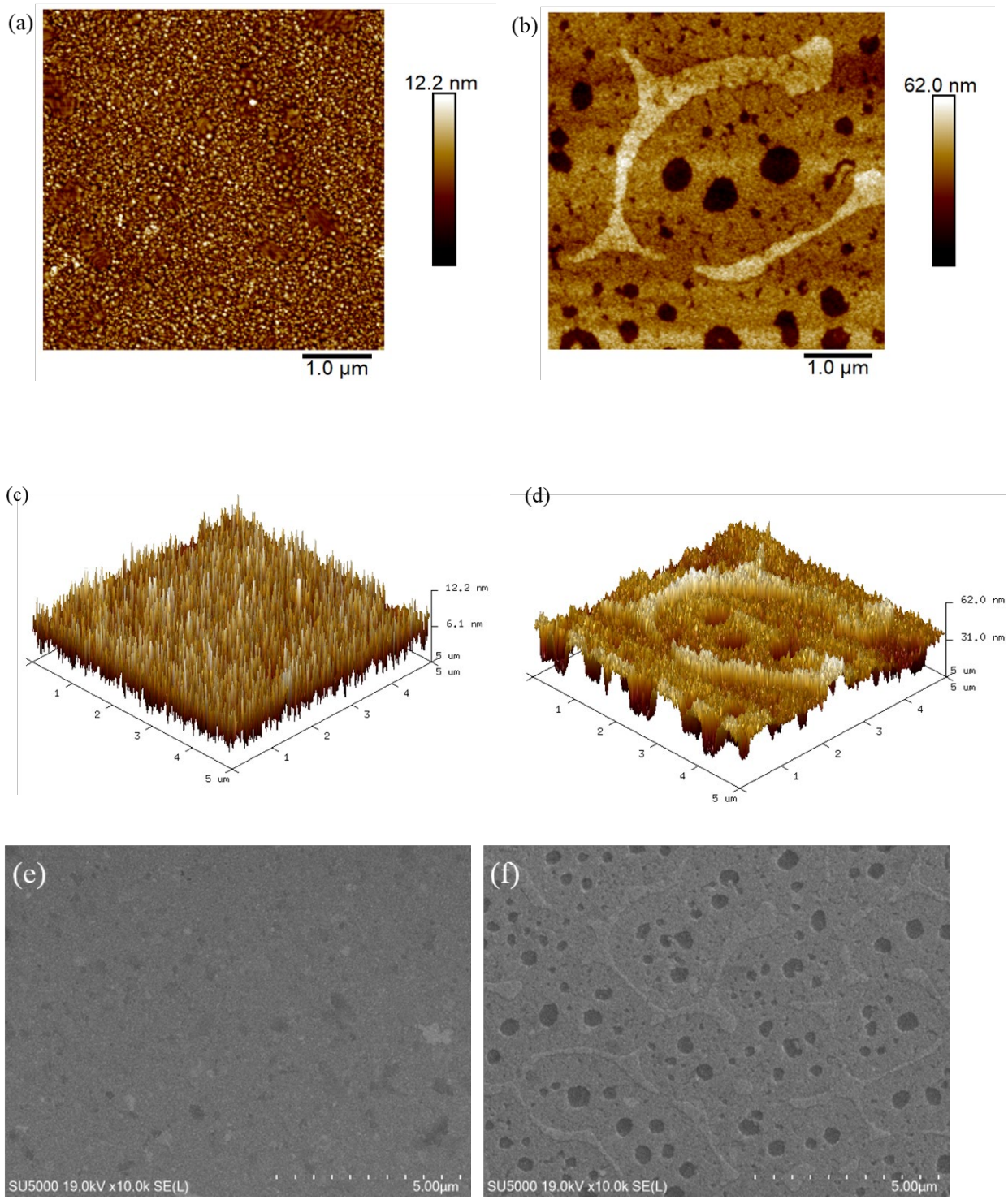


Figure 5.3. (a, b) AFM top-view, (c, d) AFM 3D, and (e, f) SEM images comparing the surface morphology of Glass/Ag and Glass/R-QDs/Ag films respectively.

Film	RMS	Lowest to highest point distance of the surface
Glass/Ag	1.75 nm	12.2 nm
Glass/R-QDs/Ag	8.15 nm	62 nm

Table 5.1. RMS values and height difference between the lowest and the highest point in the surface.

Next, we investigate the feasibility of using quenching by metals for the purpose of color patterning to fabricate QLEDs that emit two different colors, R or G, from the same QD layer stack. For this, we use an inverted QLED architecture, with ITO coated glass substrate, and ZnO coated on it, respectively serving as cathode and ETL, and with CBP, MoO3, and Al, serving as HTL, HIL, and anode, respectively, for both devices. The device fabrication process is illustrated in Figure 5.4, producing an R-QLED (device A) and a G-QLED (device B) side by side on the same substrate.

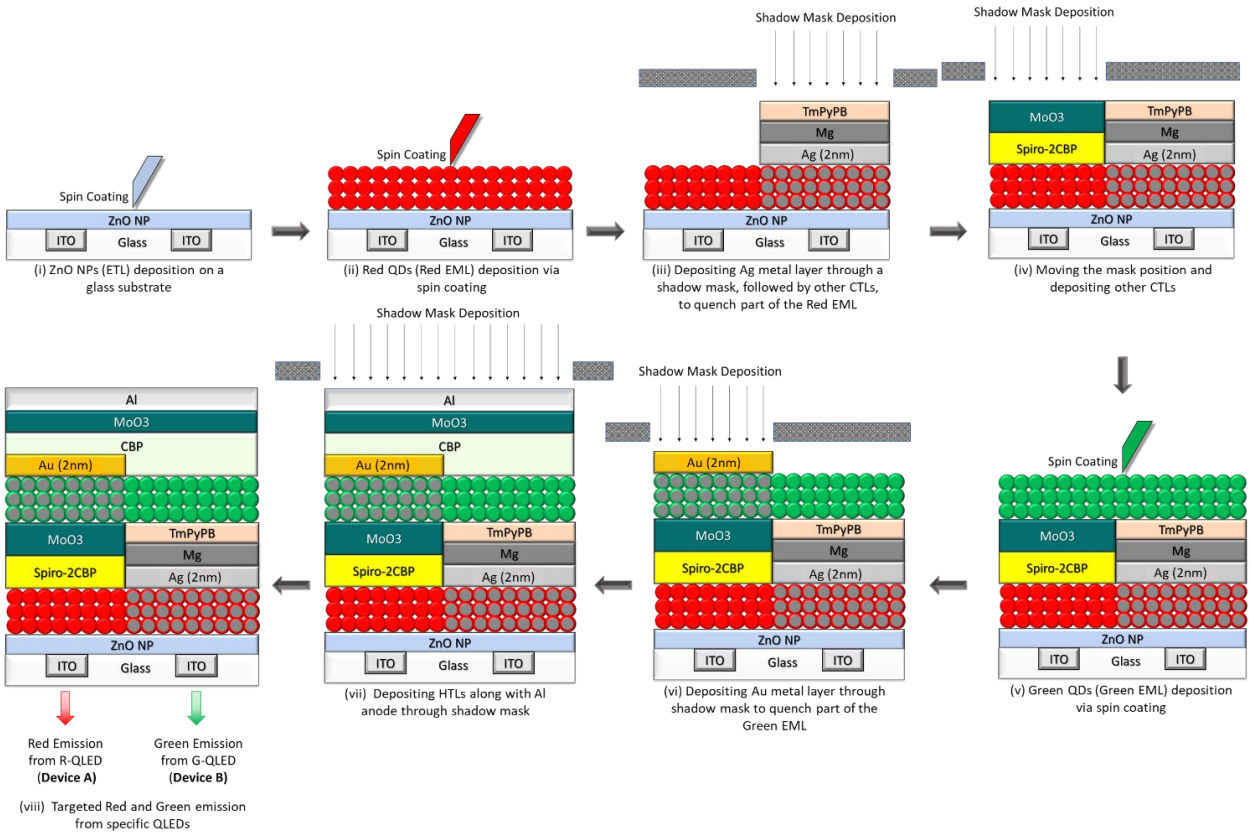
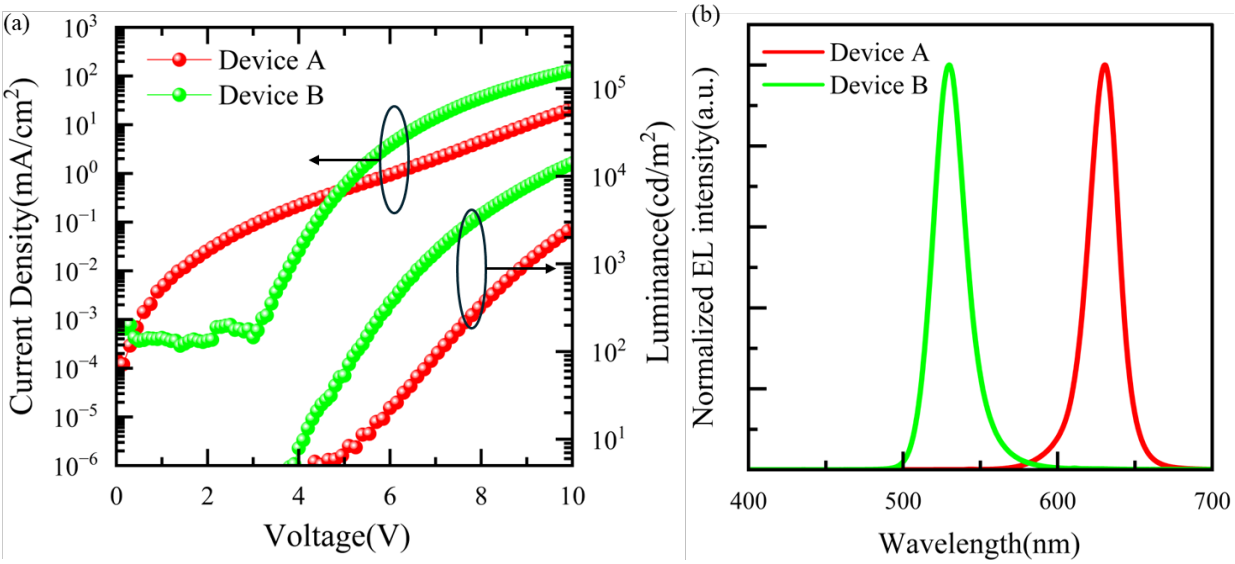


Figure 5.4. Process of the RG QLED fabrication.

The ZnO ETL and an R-QD layer are sequentially coated on the ITO coated glass substrate via spin coating respectively. Next, the substrate is placed in a vacuum chamber and 2 nm of Ag, used as a quenching metal, is deposited using thermal evaporation on one area of the R-QD layer (Area B in the figure) through a shadow mask. Mg and TmPyPB, to serve as EIL and ETL to the next G-QD layer are subsequently deposited on the same area through the same shadow mask. After this step, the shadow mask is moved to area A, and 2,7-Bis(carbazol-9-yl)-9,9-spirobifluorene (Spiro-2CBP) and MoO3, serving as HTL and HIL, respectively, for the R-QD layer in area A (i.e. device A) are deposited. The substrate is then removed from the vacuum chamber, and a G-QD layer is coated on the entire substrate via spin coating. The substrate is then moved back to the vacuum chamber, and Au with a thickness of 2 nm, used as a quenching metal

for the G-QDs is deposited, through a shadow mask, on area A. Finally, CBP, MoO3 and Al are sequentially coated on both areas. The choice of utilizing two different metals (Ag and Au) as quenching agents in different tandem structures is predicated on their different charge inject characteristics, determined by their respective work functions. In one case, the quenched layer is in the electron transport path and therefore needs to inject electrons in the subsequent layer, whereas in another case, the quenched layer is in the hole transport path and therefore needs to inject holes in the subsequent layer. Therefore, Au is selected in Device A (R-QLED) because of its favorable hole injection properties, while Ag is employed in Device B (G-QLED) due to its preferable electron injection properties.



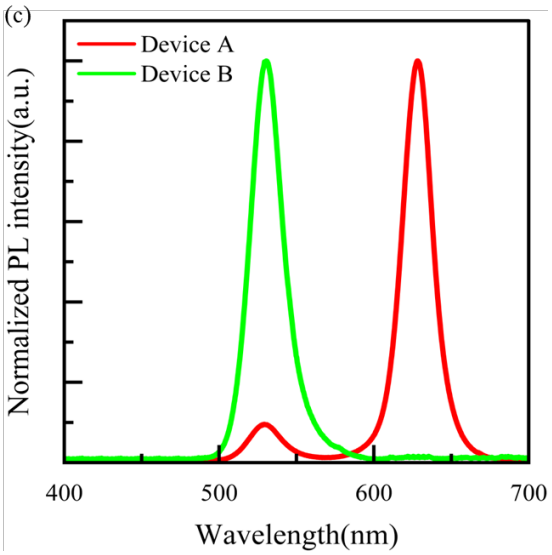


Figure 5.5. (a) J-V-L, (b) Normalized EL and (c) Normalized PL spectra collected from the two different QLEDs from the same QD layer stack.

JVL characteristics of the two devices, denoted as Device A (R-QLED) and Device B (G-QLED) are shown in Figure 5.5.a. The JVL characteristics exhibit the usual shape, indicating that the presence of metal layer in the device structures does not result in very different electrical behaviour. At 20 mA/cm^2, the driving voltage was 9.9 and 7.3V and the luminance was 2400 and 1900 cd/m^2, respectively, corresponding to a current efficiency of 8.3 and 2.3 cd/A, respectively, in the two devices, respectively. Figure 5.5.b shows the normalized EL spectra of the two devices. As can be seen, each spectrum shows a single emission, with a peak at 630 nm corresponding to red in case of device A and a peak at 530 nm corresponding to green in case of device B with no detectable parasitic emission from the other color in the two cases. The spectra prove that the use of the metals (Ag and Au) is effective in suppressing EL from the treated layers, making the stack produce only one color despite the presence of both R-QD and G-QD across the entire substrate. To test if the absence of EL from the R-QD and G-QD layers is indeed the result of metal-induced

quenching in the treated areas and not due to other process, such as for example, charge imbalance, we conduct PL measurements. Figure 5.5.c shows the PL spectra collected from devices A and B under 335 nm excitation. As can be seen, the spectrum from A shows very limited PL in the green area whereas the spectrum from B shows no detectable PL in the red area. This indicates that the EL suppression in these devices arises from metal-induced quenching of the QDs rather than from charge imbalance.

Finally, we use the same approach to create a hybrid QLED/OLED RGB preliminary demonstrator which uses QLEDs for the red and green colors, and OLEDs for the blue. The reason behind the selection of blue OLEDs instead of blue QLEDs is due to the use of an inverted device architecture, which limits the efficiency of blue QLEDs [119]. The general structure of the RGB hybrid device is schematically depicted in Figure 5.6.

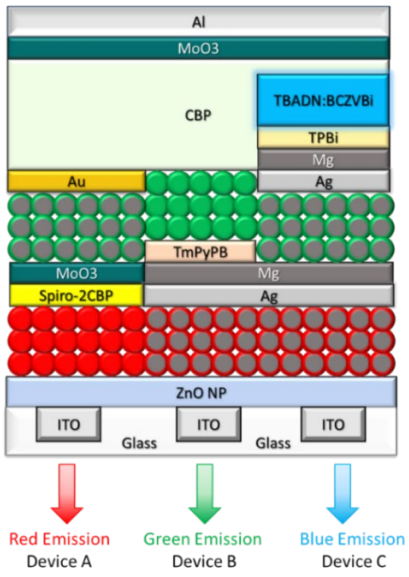
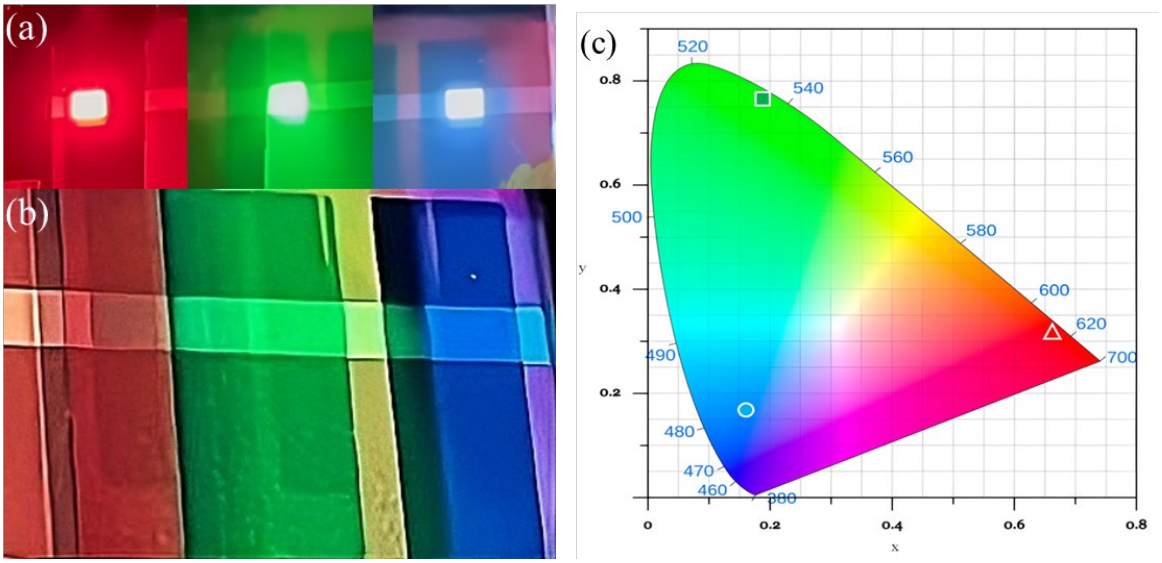


Figure 5.6. Structure of the RGB hybrid device (R, G QLEDs and B-OLED)

In these devices, the red and green QLEDs are fabricated using the same materials and processing steps as in the R and G devices described earlier, with the red and green QD layers coated by spin coating and subsequently coated with metals (Ag and Au) by thermal evaporation through shadow masks in order to achieve selective quenching in the desired areas. A blue OLED is then coated by thermal evaporation in an area where both the R- and G-QDs were coated by the quenching metals. For the blue OLED, a host : guest material system consisting of TBADN and BCzVBi is used.



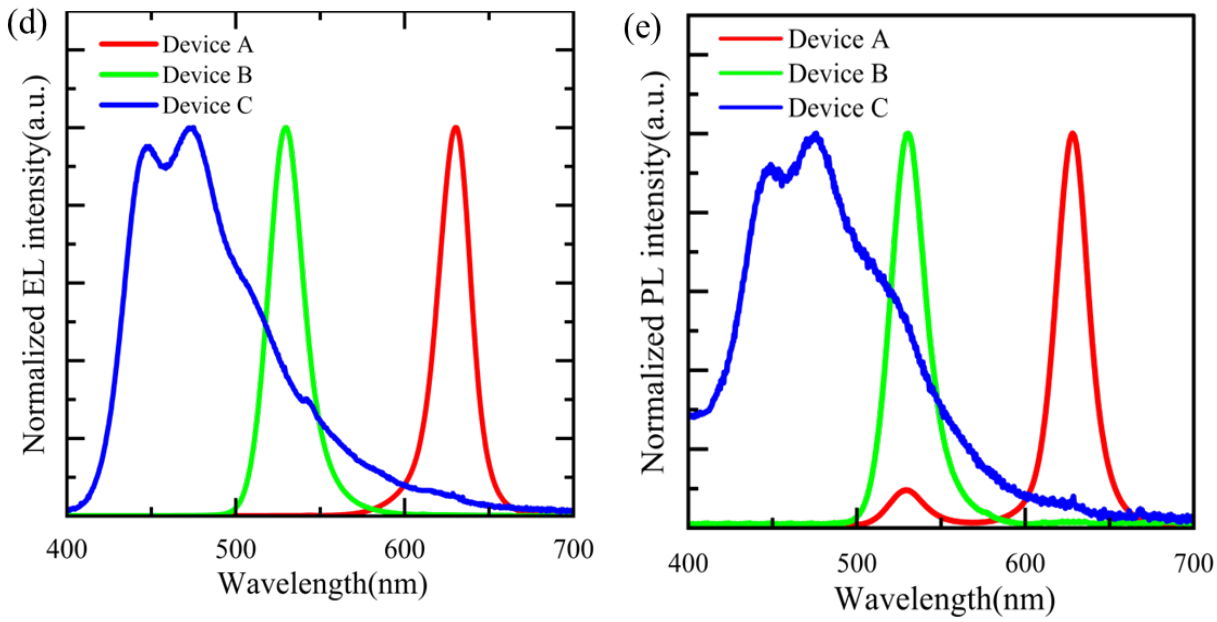


Figure 5.7. (a) EL image, (b) PL image under UV lamp of the full RGB hybrid device, (c) CIE color index of the devices (for Red X: 0.673 and Y: 0.326, for Green X: 0.195 and Y: 0.776, and for Blue X: 0.165 and Y: 187), (d) Normalized EL, and (e) Normalized PL spectra of these devices.

Figure 5.7.a and b show the EL and the PL images under UV illumination of the full RGB hybrid devices. The corresponding CIE coordinates are Red: X = 0.673, Y = 0.326; Green: X = 0.195, Y = 0.776; Blue: X = 0.165, Y = 0.187 (Figure 5.7.c). Figures 5.7.d and e respectively depict the normalized EL and the normalized PL spectra under 335 nm excitation. The EL spectra show only the characteristic emission from their respective EMLs, with no detectable parasitic emission from other layers. The PL spectra are also dominated by emission from the EML in each case, although limited green emission is observed in the spectra of the R and B devices, again pointing to efficient quenching of the R- and G-QD layers in areas coated with quenching metals. These results demonstrate the feasibility of fabricating R, G, and B devices side by side on the

same substrate. Furthermore, since the patterning is realized through thermal evaporation of metals using shadow masks, the methodology is inherently compatible with established pixel-definition processes in OLED fabrication. This indicates that similar pixel resolutions can be directly extended from OLED to QLED displays without necessitating alternative patterning strategies.

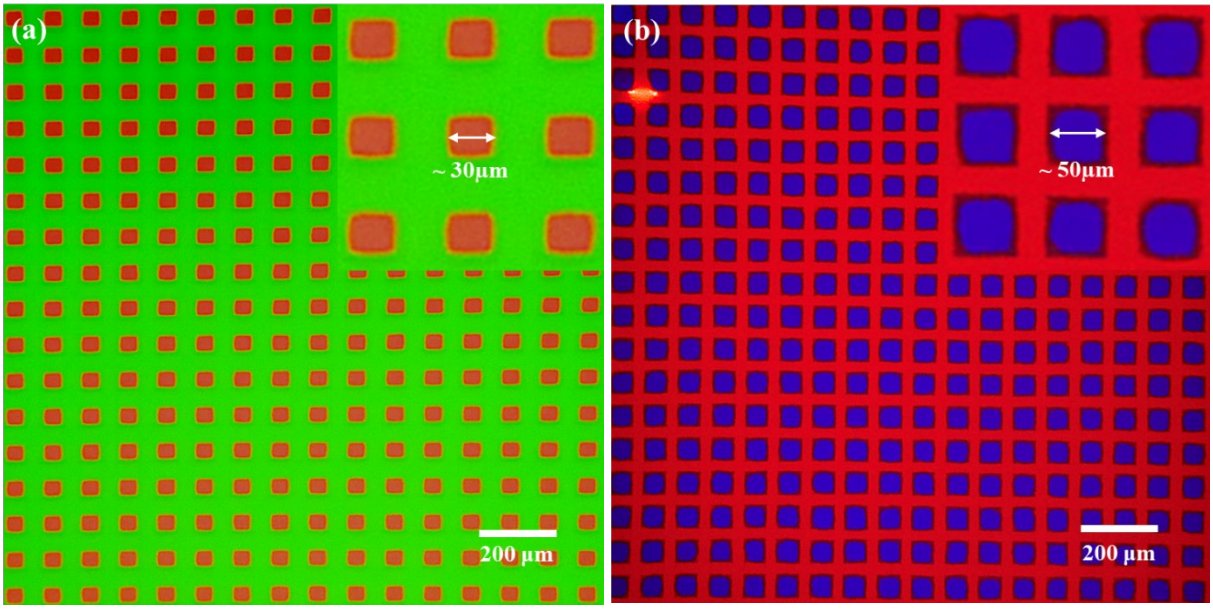


Figure 5.8. Patterned devices showing (a) side-by-side integration of red and green QLED emissive areas within a single device, and (b) side-by-side integration of red QLEDs with blue OLEDs.

Figure 5.8.a and b show the EL image of an RG QLED array, and a R QLED and B OLED hybrid array, respectively, fabricated using this patterning technique. In the first array, the QLED stack consisted of ITO/ZnO/R-QDs/ TFB/MoO_3/Au/G-QDs/CBP/MoO_3/Al. The MoO_3 and Au layers deposited prior to the G-QDs were thermally evaporated through a mesh mask, in

order to facilitate hole injection and to quench the G-QDs in selected areas. For the RB hybrid array, a device structure of ITO/ZnO/R-QDs/Ag/Mg/TPBi/TBADN:BCzVBi/CBP/MoO_3/Al was used. Here, the metal, EILs, and OLEDs were thermally evaporated through another mesh mask. The mesh mask apertures were approximately 30 μm for the RG QLED array and 50 μm for the RB hybrid array, with an inter-aperture spacing of ~50 μm. In the apertured regions of the RG QLED array device, EL emission originates from the R-QDs, whereas in areas without any metal, only emission from the G-QDs is obtained (Figure 5.8.a). Similarly, for the RB hybrid array, apertured regions yield emission from the B OLEDs, while non-apertured regions produce emission from the R-QDs (Figure 5.8.b). The arrays show well-defined feature boundaries, and emission is confined to the apertured regions, consistent with the selective deposition of metal layers through the mesh mask. The reason only two-color side-by-side patterning was demonstrated is the limitation of our laboratory setup, which does not allow accurate alignment of two sequential mesh masks on a single device. This constraint is specific to our facilities; in commercial or advanced research settings, such multi-mask alignment can be readily achieved, enabling full RGB patterned arrays. This demonstrates the feasibility of this patterning approach for microscale patterning. Taken together, these findings highlight the potential of this approach as a feasible and scalable route for RGB patterning of QLEDs into display-relevant architectures.

5.2 Conclusion

In conclusion, we have presented a novel methodology for achieving RGB color patterning in QLEDs through metal quenching enabled by shadow mask deposition technique. By selectively modulating the emission from specific color-emitting areas using metals as quenching agents, we have demonstrated precise control over the RGB color output. Further characterization

of the QD layers coated with quenching metals provided evidence suggesting the penetration of metals into the QD layers, leading to increased surface roughness and transmittance. This observation supports the theory that metal quenching involves efficient energy transfer from the excitonic state to the metal state, resulting in the quenching of excitonic states of the QDs. As this technique allows deposition of metals through shadow mask, it can facilitate higher resolution patterning of RGB pixel layers in QLED displays, where each pixel requires precise patterning of the corresponding-colored material. Also, by using this approach, more pixels can be accommodated per inch, consequently resulting in higher display resolutions compared to conventional QLED color patterning methodologies utilizing wet coating processes.

Chapter 6
Conclusions & Recommendations for Future Work

6.1 Summary of Main Conclusions

This section summarizes the main findings of this work. The fundamental objective of this research was to investigate and overcome the poor efficiency of QLEDs using organic ETLs, as well as to study the feasibility of RGB color patterning in QLEDs via metal quenching. The research was categorized into two main objectives: (i) understanding and overcoming the poor efficiency of QLEDs utilizing organic ETLs, and (ii) Testing the feasibility RGB color patterning in QLED panels via quenching by metals via a shadow mask

Objective (i): Understanding and Overcoming the Poor Efficiency of QLEDs Utilizing Organic Electron Transport Layers.

- Found out that the main cause of low efficiency in QLEDs with organic ETLs is due to excessive electron leakage to HTL from QDs-EML, rather than poor electron mobility of these ETLs.
- Found out that using multilayer ETLs with varying electron mobilities leads to the formation of negative space charge at the interfaces, which helps to suppress electron overflow, thereby reducing electron leakage and enhancing device efficiency.
- A new multilayer ETLs architecture based on organic materials was developed, resulting in record-breaking efficiencies in green and red QLEDs employing organic ETLs.

- A correlation was identified between electron leakage and hole accumulation at the QD/HTL interface.

Objective (ii): Testing the feasibility of RGB Color Patterning in QLED Panels via Quenching by Metals via a Shadow Mask.

- Found out that metal deposition causes morphological changes in the QD layer, including increased surface roughness and partial metal diffusion, both of which facilitates quenching.
- Investigated the feasibility of this patterning technique of quenching by metals through a shadow mask and successfully fabricated a hybrid RGB QLED/OLED structure that produces spatially distinct red, green, and blue emission from a uniform device stack.
- Demonstrated precise microscale patterning capability, where emission was confined within defined regions, confirming the technique's compatibility with high-resolution pixel formation.

6.2 Recommendations for Future Work

Building upon the findings of this study, several directions are recommended to further advance the understanding and performance of QLEDs using organic ETLs and to refine the scalability of the proposed patterning technique by metal quenching. For QLEDs utilizing organic ETLs, future work should focus on exploring other organic materials with lower electron mobility yet with sufficiently shallow LUMO (e.g. < 3.2 eV) to allow efficient electron injection. Additionally, interfacial engineering approaches, such as the introduction of ultrathin dielectric or

molecular dipole interlayers, could be investigated to precisely control charge injection barriers and minimize electron leakage at the QD/HTL interface. Extending the multilayer ETL strategy to blue QLEDs would also be valuable, as blue devices continue to face severe efficiency and stability limitations. Furthermore, systematic long-term operational stability tests under continuous electrical stress and varying environmental conditions should be conducted to investigate the durability and commercial feasibility of organic ETL-based QLEDs. Complementary to experimental investigations, numerical modeling of carrier transport and recombination within multilayer organic ETLs could provide deeper insights into charge dynamics and guide further optimization of layer thicknesses, energy-level alignments, and material selection.

For the patterning technique via quenching by metal, further investigation into the metal/QD interface and diffusion mechanisms is recommended to better understand how these interactions govern quenching efficiency, surface roughness, and potential degradation pathways. Advanced analytical techniques such as X-ray Photoelectron Spectroscopy (XPS) profiling or cross-sectional Transmission Electron Microscopy (TEM) could provide evidence of metal diffusion into the QD layer and interfacial reactions. Optimization of the metal deposition parameters including metal type, thickness, and deposition rate should also be investigated to achieve controllable quenching while maintaining smooth film morphology and avoiding excessive diffusion that may lead to shorting or instability. The demonstrated microscale emission confinement highlights the potential of this method for high-resolution display fabrication; therefore, expanding this work toward multi-mask or lithographically aligned patterning to achieve sub-20 μm pixel definition could be a potential next step. Additionally, investigating the operational stability and lifetime of these patterned QLEDs will be critical to assess potential trade-

offs between resolution and device robustness. Finally, integration of this patterning approach with large-area or roll-to-roll fabrication processes, as well as exploring its compatibility with hybrid or multi-modal pixel architectures, could further establish this method as a practical and scalable solution for next-generation QLED display technologies.

References

1. Peng, X., et al., *Epitaxial growth of highly luminescent CdSe/CdS core/shell nanocrystals with photostability and electronic accessibility*. Journal of the American Chemical Society, 1997. **119**(30): p. 7019-7029.
2. Murray, C., D.J. Norris, and M.G. Bawendi, *Synthesis and characterization of nearly monodisperse CdE (E= sulfur, selenium, tellurium) semiconductor nanocrystallites*. Journal of the American Chemical Society, 1993. **115**(19): p. 8706-8715.
3. Clarke, M.T., et al., *Synthesis of super bright indium phosphide colloidal quantum dots through thermal diffusion*. Communications Chemistry, 2019. **2**(1): p. 36.
4. Wang, S., et al., *Development and challenges of indium phosphide-based quantum-dot light-emitting diodes*. Journal of Photochemistry and Photobiology C: Photochemistry Reviews, 2023. **55**: p. 100588.
5. Boles, M.A., et al., *The surface science of nanocrystals*. Nature materials, 2016. **15**(2): p. 141-153.
6. Costa, M.C., et al., *Two-dimensional quantum dots: from photoluminescence to biomedical applications*. Solids, 2022. **3**(4): p. 578-602.
7. Fan, J., et al., *Recent Progress of Quantum Dots Light-Emitting Diodes: Materials, Device Structures, and Display Applications*. Advanced Materials, 2024. **36**(37): p. 2312948.
8. Protesescu, L., et al., *Nanocrystals of cesium lead halide perovskites (CsPbX3, X= Cl, Br, and I): novel optoelectronic materials showing bright emission with wide color gamut*. Nano letters, 2015. **15**(6): p. 3692-3696.
9. Brus, L.E., *Electron–electron and electron-hole interactions in small semiconductor crystallites: The size dependence of the lowest excited electronic state*. The Journal of chemical physics, 1984. **80**(9): p. 4403-4409.
10. Alivisatos, A.P., *Semiconductor clusters, nanocrystals, and quantum dots*. science, 1996. **271**(5251): p. 933-937.
11. Bera, D., et al., *Quantum dots and their multimodal applications: a review*. Materials, 2010. **3**(4): p. 2260-2345.
12. García de Arquer, F.P., et al., *Semiconductor quantum dots: Technological progress and future challenges*. Science, 2021. **373**(6555): p. eaaz8541.
13. Naylor-Adamson, L., et al., *Quantum dot imaging agents: haematopoietic cell interactions and biocompatibility*. Cells, 2024. **13**(4): p. 354.
14. Anikeeva, P.O., et al., *Quantum dot light-emitting devices with electroluminescence tunable over the entire visible spectrum*. Nano letters, 2009. **9**(7): p. 2532-2536.
15. Yuan, Q., et al., *A review on the electroluminescence properties of quantum-dot light-emitting diodes*. Organic Electronics, 2021. **90**: p. 106086.
16. Liu, Z., et al., *Micro-light-emitting diodes with quantum dots in display technology*. Light: Science & Applications, 2020. **9**(1): p. 83.
17. Luo, Z., Y. Chen, and S.-T. Wu, *Wide color gamut LCD with a quantum dot backlight*. Optics express, 2013. **21**(22): p. 26269-26284.

18. Bang, S.Y., et al., *Technology progress on quantum dot light-emitting diodes for next-generation displays*. Nanoscale Horizons, 2021. **6**(2): p. 68-77.
19. Li, M., et al., *Ultrabright and stable top-emitting quantum-dot light-emitting diodes with negligible angular color shift*. Nature Communications, 2024. **15**(1): p. 5161.
20. Lee, T., et al., *Highly efficient and bright inverted top-emitting InP quantum dot light-emitting diodes introducing a hole-suppressing interlayer*. Small, 2019. **15**(50): p. 1905162.
21. Li, D., et al., *Enhancing performance of inverted quantum-dot light-emitting diodes based on a solution-processed hole transport layer via ligand treatment*. Journal of Semiconductors, 2023. **44**(9): p. 092603.
22. Shang, Y. and Z. Ning, *Colloidal quantum-dots surface and device structure engineering for high-performance light-emitting diodes*. National Science Review, 2017. **4**(2): p. 170-183.
23. Dabbousi, B.O., et al., *(CdSe) ZnS core− shell quantum dots: synthesis and characterization of a size series of highly luminescent nanocrystallites*. The Journal of Physical Chemistry B, 1997. **101**(46): p. 9463-9475.
24. Fu, Y., et al., *Excellent stability of thicker shell CdSe@ ZnS/ZnS quantum dots*. RSC advances, 2017. **7**(65): p. 40866-40872.
25. Brown, R.P., et al., *Synthesis and degradation of cadmium-free InP and InPZn/ZnS quantum dots in solution*. Langmuir, 2018. **34**(46): p. 13924-13934.
26. Singh, R.K., et al., *Progress of backlight devices: emergence of halide perovskite quantum dots/nanomaterials*. Frontiers in Nanotechnology, 2022. **4**: p. 863312.
27. Li, Z., et al., *Carrier dynamics in alloyed chalcogenide quantum dots and their light-emitting devices*. Advanced Energy Materials, 2021. **11**(40): p. 2101693.
28. Kim, H.-M., et al., *Li and Mg Co-doped zinc oxide electron transporting layer for highly efficient quantum dot light-emitting diodes*. ACS applied materials & interfaces, 2018. **10**(28): p. 24028-24036.
29. Park, M., et al., *QD light-emitting diodes: an overview and their impact on the display landscape*. Information Display, 2024. **40**(3): p. 32-37.
30. Huang, Y., et al., *Advances in quantum-dot-based displays, Nanomaterials 10 (2020) 1327*.
31. Tian, D., et al., *A review on quantum dot light-emitting diodes: from materials to applications*. Advanced Optical Materials, 2023. **11**(2): p. 2201965.
32. Zheng, Y., et al., *Ultra-bright and energy-efficient quantum-dot LEDs by idealizing charge injection*. arXiv preprint arXiv:2406.09730, 2024.
33. Han, C.-Y. and H. Yang, *Development of colloidal quantum dots for electrically driven light-emitting devices*. Journal of the Korean Ceramic Society, 2017. **54**(6): p. 449-469.
34. Chen, D., et al., *Shelf-stable quantum-dot light-emitting diodes with high operational performance*. Advanced Materials, 2020. **32**(52): p. 2006178.
35. Huang, Y.-M., et al., *Advances in quantum-dot-based displays*. Nanomaterials, 2020. **10**(7): p. 1327.
36. Kim, J., et al., *Recent advances and challenges of colloidal quantum dot light-emitting diodes for display applications*. Advanced Materials, 2024. **36**(20): p. 2212220.

37. Baek, G.W., et al., *Optimum Design Configuration of Thin-Film Transistors and Quantum-Dot Light-Emitting Diodes for Active-Matrix Displays*. Advanced Materials, 2023. **35**(48): p. 2304717.
38. Baek, G.W., et al., *Progress in the development of active-matrix quantum-dot light-emitting diodes driven by non-Si thin-film transistors*. Materials, 2022. **15**(23): p. 8511.
39. Kajiyama, Y., *New Color Patterning Techniques for OLED Displays*. 2015, University of Waterloo Waterloo, France.
40. Kim, C., et al., *Fine metal mask material and manufacturing process for high-resolution active-matrix organic light-emitting diode displays*. Journal of the Society for Information Display, 2020. **28**(8): p. 668-679.
41. Reineke, S., et al., *White organic light-emitting diodes: Status and perspective*. Reviews of Modern Physics, 2013. **85**(3): p. 1245-1293.
42. Zhang, L., et al., *Strategies to achieve high-performance white organic light-emitting diodes*. Materials, 2017. **10**(12): p. 1378.
43. Li, G., et al., *Color-conversion displays: current status and future outlook*. Light: Science & Applications, 2024. **13**(1): p. 301.
44. Chen, L., et al., *A magnetic metal hard mask on silicon substrate for direct patterning ultra-high-resolution OLED displays*. Micromachines, 2022. **13**(7): p. 997.
45. Lee, J.Y., B.-K. Ju, and K.H. Cho, *High-resolution patterning of organic emitting-layer by using inkjet printing and sublimation transfer process*. Nanomaterials, 2022. **12**(9): p. 1611.
46. Lee, S., et al., *Micrometer-scale indirect photopatterning of RGB OLED emissive layers in single phase network structure*. Light: Science & Applications, 2025. **14**(1): p. 247.
47. Chrzanowski, M., et al., *Effect of air exposure of ZnMgO nanoparticle electron transport layer on efficiency of quantum-dot light-emitting diodes*. ACS Applied Materials & Interfaces, 2021. **13**(17): p. 20305-20312.
48. Ye, Z., et al., *Solution-processed quantum-dot light-emitting diodes combining ultrahigh operational stability, shelf stability, and luminance*. npj Flexible Electronics, 2022. **6**(1): p. 96.
49. Wang, S., et al., *Operando ZnO recrystallization for efficient quantum-dot light-emitting diodes*. Light: Science & Applications, 2025. **14**(1): p. 196.
50. Bastola, A., et al., *Formulation of functional materials for inkjet printing: A pathway towards fully 3D printed electronics*. Materials Today Electronics, 2023. **6**: p. 100058.
51. Eun, Y.-B., et al., *Performance improvement of quantum dot light-emitting diodes using a ZnMgO electron transport layer with a core/shell structure*. Materials, 2023. **16**(2): p. 600.
52. Cai, F., et al., *Defect passivation and electron band energy regulation of a ZnO electron transport layer through synergetic bifunctional surface engineering for efficient quantum dot light-emitting diodes*. Nanoscale, 2023. **15**(25): p. 10677-10684.
53. Barnes, B.K. and K.S. Das, *Resistance switching and memristive hysteresis in visible-light-activated adsorbed ZnO thin films*. Scientific reports, 2018. **8**(1): p. 2184.

54. He, S., et al., *Anomalous efficiency elevation of quantum-dot light-emitting diodes induced by operational degradation*. Nature Communications, 2023. **14**(1): p. 7785.
55. Su, Q., et al., *Origin of positive aging in quantum-dot light-emitting diodes*. Advanced Science, 2018. **5**(10): p. 1800549.
56. Chen, Z. and S. Chen, *Eliminating Positive Aging in Quantum Dot Light-Emitting Diodes by H2O-Treatment*. Advanced Materials, 2025: p. 2503477.
57. Lee, K., et al., *Understanding of the aging pattern in quantum dot light-emitting diodes using low-frequency noise*. Nanoscale, 2020. **12**(29): p. 15888-15895.
58. Jang, H., et al., *Positive aging in InP-based QD-LEDs encapsulated with epoxy: the role of thiol molecules and post-annealing treatment*. Journal of Materials Chemistry C, 2023. **11**(41): p. 14292-14298.
59. Tominov, R.V., et al., *Nanoscale-resistive switching in forming-free zinc oxide memristive structures*. Nanomaterials, 2022. **12**(3): p. 455.
60. Gul, F. and H. Efeoglu, *ZnO and ZnO1− x based thin film memristors: The effects of oxygen deficiency and thickness in resistive switching behavior*. Ceramics International, 2017. **43**(14): p. 10770-10775.
61. Kara, R., L. Mentar, and A. Azizi, *Synthesis and characterization of Mg-doped ZnO thin-films electrochemically grown on FTO substrates for optoelectronic applications*. RSC advances, 2020. **10**(66): p. 40467-40479.
62. Ding, S., et al., *Impact of the resistive switching effects in ZnMgO electron transport layer on the aging characteristics of quantum dot light-emitting diodes*. Applied Physics Letters, 2020. **117**(9).
63. Wang, Y., et al., *Study on electron transport characterization in TPBi thin films and OLED application*. The Journal of Physical Chemistry C, 2021. **125**(30): p. 16753-16758.
64. Mude, N.N., et al., *An efficient organic and inorganic hybrid interlayer for high performance inverted red cadmium-free quantum dot light-emitting diodes*. Nanoscale Advances, 2022. **4**(3): p. 904-910.
65. Lee, W., et al., *Polyethylenimine-ethoxylated dual interfacial layers for highly efficient and all-solution-processed inverted quantum dot light-emitting diodes*. Optics Express, 2020. **28**(23): p. 33971-33981.
66. Chae, Y.-B., et al., *Enhancing efficiency in inverted quantum dot light-emitting diodes through arginine-modified ZnO nanoparticle electron injection layer*. Nanomaterials, 2024. **14**(3): p. 266.
67. Kim, J.-H. and J.-W. Park, *Designing an electron-transport layer for highly efficient, reliable, and solution-processed organic light-emitting diodes*. Journal of Materials Chemistry C, 2017. **5**(12): p. 3097-3106.
68. Morab, S., M.M. Sundaram, and A. Pivrikas, *Review on charge carrier transport in inorganic and organic semiconductors*. Coatings, 2023. **13**(9): p. 1657.
69. Zhao, Y.-Y., et al., *Improved performance of CsPbBr3 quantum-dot light-emitting diodes by bottom interface modification*. Organic Electronics, 2022. **109**: p. 106620.
70. Naqvi, S.M.K.A., et al., *Unraveling degradation processes and strategies for enhancing reliability in organic light-emitting diodes*. Nanomaterials, 2023. **13**(23): p. 3020.

71. Zhao, J., et al., *Large-area patterning of full-color quantum dot arrays beyond 1000 pixels per inch by selective electrophoretic deposition*. Nature Communications, 2021. **12**(1): p. 4603.
72. Bai, J., et al., *Achieving high performance InP quantum dot light-emitting devices by using inkjet printing*. Organic Electronics, 2023. **113**: p. 106705.
73. Wei, C., et al., *Highly ordered inkjet-printed quantum-dot thin films enable efficient and stable QLEDs with EQE exceeding 23%*. Escience, 2024. **4**(3): p. 100227.
74. Jiang, C., et al., *Coffee-ring-free quantum dot thin film using inkjet printing from a mixed-solvent system on modified ZnO transport layer for light-emitting devices*. ACS applied materials & interfaces, 2016. **8**(39): p. 26162-26168.
75. Yang, K.P., et al., *Coffee ring-free inkjet printing using UV-curable quantum dot-acrylate solution for high resolution displays*. Colloids and Surfaces A: Physicochemical and Engineering Aspects, 2024. **697**: p. 134313.
76. Gong, Z., et al., *Fluid Dynamics of Quantum Dot Inks: Non-Newtonian Behavior and Precision Control in Advanced Printing*. Fluid Dynamics & Materials Processing, 2025. **21**(9).
77. Hu, Z., et al., *Inkjet printed uniform quantum dots as color conversion layers for full-color OLED displays*. Nanoscale, 2020. **12**(3): p. 2103-2110.
78. Park, S.Y., et al., *Patterning quantum dots via photolithography: a review*. Advanced Materials, 2023. **35**(41): p. 2300546.
79. Chen, Z., et al., *Research progress of quantum dot photolithography patterning and direct photolithography application*. Nano Research, 2024. **17**(12): p. 10386-10411.
80. Sharp, K.G., et al., *Effect of stamp deformation on the quality of microcontact printing: theory and experiment*. Langmuir, 2004. **20**(15): p. 6430-6438.
81. Eichinger, C.D., T.W. Hsiao, and V. Hlady, *Multiprotein microcontact printing with micrometer resolution*. Langmuir, 2012. **28**(4): p. 2238-2243.
82. Mkhize, N. and H. Bhaskaran, *Electrohydrodynamic jet printing: Introductory concepts and considerations*. Small Science, 2022. **2**(2): p. 2100073.
83. Cai, N., et al., *Error analysis and correction for electrohydrodynamic printing: a review*. 3D Printing and Additive Manufacturing, 2024.
84. Delaporte, P. and A.-P. Alloncle, *Laser-induced forward transfer: A high resolution additive manufacturing technology*. Optics & Laser Technology, 2016. **78**: p. 33-41.
85. Jalaal, M., et al., *Destructive mechanisms in laser induced forward transfer*. Applied physics letters, 2019. **114**(21).
86. Cao, Y., et al., *Review of industrialization development of nanoimprint lithography technology*. Chips, 2025. **4**(1): p. 10.
87. Scott, S.M. and Z. Ali, *Fabrication methods for microfluidic devices: An overview*. Micromachines, 2021. **12**(3): p. 319.
88. Jiang, L. and M. Feldman. *Accurate alignment technique for nanoimprint lithography*. in *Metrology, Inspection, and Process Control for Microlithography XIX*. 2005. SPIE.
89. Shen, H., et al., *High-efficiency, low turn-on voltage blue-violet quantum-dot-based light-emitting diodes*. Nano letters, 2015. **15**(2): p. 1211-1216.
90. Chen, B., D. Li, and F. Wang, *InP quantum dots: synthesis and lighting applications*. Small, 2020. **16**(32): p. 2002454.

91. Shan, Q., et al., *Perovskite quantum dots for the next-generation displays: progress and prospect*. Advanced Functional Materials, 2024. **34**(36): p. 2401284.
92. Zhu, S., et al., *The photoluminescence mechanism in carbon dots (graphene quantum dots, carbon nanodots, and polymer dots): current state and future perspective*. Nano research, 2015. **8**(2): p. 355-381.
93. Chen, O., et al., *Compact high-quality CdSe–CdS core–shell nanocrystals with narrow emission linewidths and suppressed blinking*. Nature materials, 2013. **12**(5): p. 445-451.
94. Liu, Z., et al., *Colloidal quantum Dot materials and devices: A quarter-century of advances*. Light Science Applied, 2020. **9**.
95. Zhang, Y., et al., *Photoexcited carrier dynamics in colloidal quantum dot solar cells: insights into individual quantum dots, quantum dot solid films and devices*. Chemical Society Reviews, 2020. **49**(1): p. 49-84.
96. Mobarak, B. and H. Aziz, *Understanding and Overcoming the Poor Efficiency of QLEDs Utilizing Organic Electron Transport Layers*. Advanced Electronic Materials, 2025: p. e00412.
97. Xu, Q., et al., *Improved efficiency of all-inorganic quantum-dot light-emitting diodes via interface engineering*. Frontiers in Chemistry, 2020. **8**: p. 265.
98. Yokoyama, D., et al., *Molecular Stacking Induced by Intermolecular C–H⋯ N Hydrogen Bonds Leading to High Carrier Mobility in Vacuum-Deposited Organic Films*. Advanced Functional Materials, 2011. **21**(8): p. 1375-1382.
99. Sasabe, H., et al., *2-Phenylpyrimidine skeleton-based electron-transport materials for extremely efficient green organic light-emitting devices*. Chemical Communications, 2008(44): p. 5821-5823.
100. Chen, D., S.-J. Su, and Y. Cao, *Nitrogen heterocycle-containing materials for highly efficient phosphorescent OLEDs with low operating voltage*. Journal of Materials Chemistry C, 2014. **2**(45): p. 9565-9578.
101. Wang, Q. and H. Aziz, *Degradation of organic/organic interfaces in organic light-emitting devices due to polaron–exciton interactions*. ACS applied materials & interfaces, 2013. **5**(17): p. 8733-8739.
102. Yadav, R.A.K., et al., *Role of molecular orbital energy levels in OLED performance*. Scientific reports, 2020. **10**(1): p. 9915.
103. Azadinia, M., et al., *Differences in electron and hole injection and auger recombination between red, green, and blue CdSe-based quantum dot light emitting devices*. ACS nano, 2024. **18**(2): p. 1485-1495.
104. Chung, D.S., et al., *Significant lifetime enhancement in QLEDs by reducing interfacial charge accumulation via fluorine incorporation in the ZnO electron transport layer*. Nano-Micro Letters, 2022. **14**(1): p. 212.
105. Su, Q., Z. Chen, and S. Chen, *Tracing the electron transport behavior in quantum-dot light-emitting diodes via single photon counting technique*. Nature Communications, 2024. **15**(1): p. 8150.
106. Sun, X., et al., *Hole-injection-barrier effect on the degradation of blue quantum-dot light-emitting diodes*. ACS nano, 2024. **18**(7): p. 5898-5906.

107. Yan, X., et al., *Elucidating the Impact of Electron Accumulation in Quantum-Dot Light-Emitting Diodes*. Nano Letters, 2024. **24**(42): p. 13374-13380.
108. Chen, J., et al., *Influence of Encapsulation on the Efficiency and Positive Aging Behavior in Blue Quantum Dot Light-Emitting Devices*. ACS Applied Materials & Interfaces, 2023. **15**(28): p. 34240-34248.
109. Yang, L., et al., *High-performance red quantum-dot light-emitting diodes based on organic electron transporting layer*. Advanced Functional Materials, 2021. **31**(6): p. 2007686.
110. Park, M., et al., *Improving Performance of Inverted Blue Quantum-Dot Light-Emitting Diodes by Adopting Organic/Inorganic Double Electron Transport Layers*. physica status solidi (RRL)–Rapid Research Letters, 2020. **14**(5): p. 1900737.
111. Azadinia, M. and H. Aziz, *Deciphering the Causes of the Rapid Electroluminescence Loss in Blue Quantum Dot Light-Emitting Devices*. Advanced Optical Materials, 2025. **13**(4): p. 2402271.
112. Barltrop, J.A. and J.D. Coyle, *Principles of photochemistry*. (No Title), 1978.
113. Agranovich, V. and A. Mal'shukov, *Metal quenching of excitons and properties of excited states at a metal—dielectric contact*. Chemical Physics Letters, 1976. **43**(2): p. 221-223.
114. Johnson, P.B. and R.-W. Christy, *Optical constants of the noble metals*. Physical review B, 1972. **6**(12): p. 4370.
115. Güleroğlu, G. and C. Ünlü, *Spectroscopic investigation of defect-state emission in CdSe quantum dots*. Turkish Journal of Chemistry, 2021. **45**(3): p. 520-527.
116. Pietryga, J.M., et al., *Spectroscopic and device aspects of nanocrystal quantum dots*. Chemical reviews, 2016. **116**(18): p. 10513-10622.
117. Voorhees, P.W., *Ostwald ripening of two-phase mixtures*. Annual Review of Materials Science, 1992. **22**(1): p. 197-215.
118. Qian, Y., et al., *Crystallization of nanoparticles induced by precipitation of trace polymeric additives*. Nature communications, 2021. **12**(1): p. 2767.
119. Li, S.-N., et al., *Advances in solution-processed blue quantum dot light-emitting diodes*. Nanomaterials, 2023. **13**(10): p. 1695.